

A SURVEY OF PLANETARY NEBULAE IN THE SOUTHERN GALACTIC BULGE

SYLVIE F. BEAULIEU,¹ MICHAEL A. DOPITA, AND KENNETH C. FREEMAN

Mount Stromlo and Siding Spring Observatories, The Australian National University, Canberra ACT 2611, Australia; beaulieu@ast.cam.ac.uk;
Michael.Dopita, kcf@mso.anu.edu.au

Received 1998 August 6; accepted 1998 November 23

ABSTRACT

We present the results of a deep and uniform narrowband $H\alpha$ imaging survey for planetary nebulae (PNs) in the southern Galactic bulge. In our survey, we have found 56 new PNs and have rediscovered 45 known PNs. We have measured the radial velocities of this uniformly selected sample and have also remeasured radial velocities for a subset of 317 PNs from the Acker catalog. Using the COBE/DIRBE 1.25, 2.2, and 3.5 μm images, we show that there is a similar longitude distribution of the PNs and the COBE light in the zone of our deep survey. Also, we find that the extinction in our surveyed fields is not severe and that its distribution is fairly uniform. Finally, we present $H\alpha$ fluxes for 47 of our 56 newly discovered PNs and estimate the survey detection limit.

Subject headings: ISM: kinematics and dynamics — planetary nebulae: general — surveys

1. INTRODUCTION

It is estimated that the Galaxy contains between 10^4 and 4×10^4 planetary nebulae (PNs; Pottasch 1992). Only a small fraction of these PNs have been detected so far. The Strasbourg-ESO Catalogue of Galactic Planetary Nebulae (Acker et al. 1992) reports that 1820 objects have been at least once classified as PNs and that 1143 of those are considered true or probable PNs. We note that, since the completion of our study, a supplement of the catalog has been published (Acker et al. 1996) and reports an additional 384 new true, probable, and possible PNs (including the discoveries from this study).

Apart from a few serendipitous discoveries of PNs, most of them were found through important but incomplete surveys using the objective prism technique (Minkowski 1965) and photographic plates (i.e., the Palomar Survey and the ESO Survey). Some surveys were conducted in the radio continuum (Ratag 1990). The launch of the *Infrared Astronomical Satellite (IRAS)* in 1984 ushered in a new way of selecting candidates through the far-infrared excess associated with the warm dust in the nebulae. This produced a fair number of new discoveries (Ratag 1990; van de Steene 1995). Nonetheless, these surveys are still incomplete. In the case of photographic plates and objective prism surveys, faint nebulae and compact young PNs will not be detected. With *IRAS*, although it has the capability to detect objects in regions of high extinction, it is more likely to detect the dusty PNs. If a PN has a low dust density (as is more likely for old PNs), it will not be detected by *IRAS*.

Because PNs are strong emitters in $H\alpha$ and $[\text{O III}]$, we decided to conduct a deep and uniform emission-line survey for PNs in a large region of the bulge, measure their radial velocities, and then use the kinematical data to test dynamical models of the bulge (Beaulieu, Kalnajs, & Freeman 1998). This paper describes the procedure we followed in order to discover new PNs. We start with the data acquisition and reduction of the optical imaging survey (§ 2), followed by the optical spectroscopy survey and a search of the *IRAS/PSC* (§ 3). In § 4, we derive the $H\alpha$ fluxes of the newly discovered PNs using higher resolution imaging data. We then summarize and conclude in § 5.

2. THE 1.0 METER SURVEY

Most PNs emit strongly in the $[\text{O III}] \lambda\lambda 4959, 5007$ and the $H\alpha \lambda 6563$ lines. However, since an $[\text{O III}]$ line survey would be more affected by both the moonlight (more scattering) and the interstellar extinction, which can be very large in the direction of the bulge, the $H\alpha$ line was chosen instead. We also considered using the $[\text{S III}]$ line at 9530 Å. Although this line would perform very well in situations of higher interstellar extinction and brighter moonlight, it lies in a region where CCDs have lower quantum efficiency, and this would have significantly increased the time required for our survey.

The Low-Dispersion Survey Spectrograph (LDSS) of the Anglo-Australian Observatory (AAO) was attached to the 1.0 m telescope of Mount Stromlo and Siding Spring Observatories and was used as a focal reducer (without grism). This instrument, with 100 mm diameter interference filters and a 1024×1024 CCD, gives a useful circular field of $30'$ at $2''.35 \text{ pixel}^{-1}$. Throughout the survey, several CCDs were used, depending on their availability. A list of all the CCDs used can be found in Table 1, with their characteristics: the MSSSO Dewar identification (col. [1]), the CCD type (col. [2]), the physical size in pixels (col. [3]), the pixel size (col. [4]), the readout noise (col. [5]), and the electronic gain (col. [6]).

The $H\alpha$ filter was designed for a central wavelength at 6590 Å. In order to obtain an effective central wavelength of $H\alpha \lambda 6563 \text{ Å}$, we tilted the filter at a 5° angle to the optical axis of the instrument. For the nearby continuum associated with the $H\alpha$, we used an Omega 6450 Å filter. A detailed list of all the filters used can be found in Table 2, with their characteristics: the filter identification (col. [1]), the type and size (col. [2]), the central wavelength in Å (col. [3]), the filter passband in Å (col. [4]), the tilt angle (col. [5]), and the central wavelength after tilt (col. [6]).

The $H\alpha$ filter was positioned in the aperture plate holder, which is situated at the focal plane. At this position, there is enough free space to allow the filter to be tilted, and it has the further advantage that all beams have a similar angle of incidence at the filter, so the effective passband does not vary over the field. This is not the case at the pupil plane, which is the alternative filter position in the LDSS. A disadvantage of putting the filters at the focal plane is that the diameter of the field of view is about $10'$ smaller than it

¹ Present address: Institute of Astronomy, University of Cambridge, Madingley Road, Cambridge CB3 0HA, England, UK.

TABLE 1
CCD CHARACTERISTICS

CCD Number	Type	Size	Pixel (μm)	RN	Gain (e^-)
4	TEK-UV thin	1024 \times 1024	24	5.9	1
6	LGEC-E2	2186 \times 1152	22.5	5	1
9	TEK-E1 thin	1024 \times 1024	24	24	1
11	TEK-E2 thin	1024 \times 1024	24	7	1

would be if the same filter were located in the pupil plane. The continuum filter can be placed at the pupil plane, because the precise passband is of less importance for this filter.

In our study, we are interested in the PNs of the bulge and particularly the PNs at higher Galactic latitude because of their importance for investigating the dynamics of the boxy/bar regions. The COBE/DIRBE maps (Weiland et al. 1993) indicate that the most obvious regions of the Galactic bulge cover the regions of Galactic longitude $l = \pm 15^\circ$ and Galactic latitude $b = \pm 10^\circ$. Because of time restrictions, it was not possible to survey this entire bulge region. We have chosen to survey the southern part: $l = \pm 20^\circ$ and from $b = -5^\circ$ to -10° because of its lower extinction relative to the northern bulge. The choice of surveying the longitude region outside the COBE bulge is intended to provide us with data for the transition from the bulge to the disk.

Figure 1 is an optical image of the Galactic bulge taken at ESO (Madsen & Laustsen 1986; see also Fig. 1 of Wyse, Gilmore, & Franx 1997). The patchy extinction in the plane of the Galaxy is obvious. We have outlined the region covered by our survey in the southern part of the Galactic bulge.

Our field of view being $30'$ and the survey region being still quite extended, it was not possible to carry a complete and systematic coverage with overlapping fields. Statistically speaking, this is not a problem, since we want a large uniform coverage in space and depth. By uniformly spacing our $30'$ field of view over the area $l = \pm 20^\circ$ and from $b = -5^\circ$ to -10° , we produced a grid of 488 fields. In two seasons of observation, we covered 94% of the grid (458 fields). Although there were no plans to observe the northern part of the Galactic bulge, we did obtain 40 fields in the equivalent northern Galactic latitude strip, from $b = +5^\circ$ to $+10^\circ$. In early May (beginning of the bulge season in the southern hemisphere), the southern part becomes accessible only 3 hr after dusk, and we used the first 3 hr of the nights during that period for these northern fields.

In Figure 2, the filled circles represent the fields we have observed. The three empty regions in the southern grid are the 30 remaining fields, which were unobserved because of a lack of time. Each circular field covers roughly half of the total area associated with each grid point, and, added

together, they represent about 1% of the total COBE light.

In addition, we imaged 15 fields in [O III] $\lambda 5007$ (during dark time). Most PNs are strong emitters in [O III], and we wanted to test the possibility of finding more candidates by using this line, which is widely used for surveys of extragalactic PNs. The [O III] filter was combined with a BG40 blocking filter in order to block its red leak. Again, this filter was designed for a central wavelength of 5020 \AA and so needed to be tilted at a 4° angle to the optic axis in order to obtain the central wavelength for [O III] $\lambda 5007$. For the nearby continuum, we used an Omega 4750 \AA filter (Table 2).

Two exposures in H α of 500 s and one exposure in the nearby continuum of 300 s were taken. The same procedure was applied for the 15 fields in [O III]. The two exposures in H α and in [O III] were necessary to ensure removal of cosmic rays. Typical sky counts for the H α were 75–150 counts pixel $^{-1}$ (depending on the presence of moonlight) and about twice this level for the continuum.

During the two observing seasons, we were allocated a total of 72 nights at the 1.0 m telescope with a success rate of clear nights (not necessarily photometric) of 57%. A summary of the observing log can be found in Table 3, given as follows: the period covered in each observing run (col. [1]), the number of nights run $^{-1}$ (col. [2]), the proportion of clear nights run $^{-1}$ (col. [3]), and the CCD used during each run (col. [4]).

2.1. Data Reduction

The basic reduction (bias subtraction and flat-fielding) was performed using the standard IRAF techniques (Gilliland 1992; Massey 1992). Calibration images of approximately 10 bias, one dark and twilight flat fields (in each wavelength band) were obtained each night. Twilight flat fields were obtained at dusk and dawn whenever possible.

For each image, the electronic bias level was removed to first order by fitting a Chebyshev function to the overscan region and then subtracting it from each column. In order to remove any remaining bias structure, a master bias frame was created by averaging the 10 bias frames using a MINMAX rejection algorithm and then subtracting it from

TABLE 2
FILTER DETAILS

Filter	Type	λ_c	$\Delta\lambda$	Tilt	λ_c with Tilt
H α	Coherent/scientific 100 mm	6590	19	5°	6563
[O III]	Coherent/scientific 100 mm	5020	40	4°	5007
Continuum	Omega 100 mm	6450	42	0°	6450
Continuum	Omega 100 mm	4750	40	0°	4750

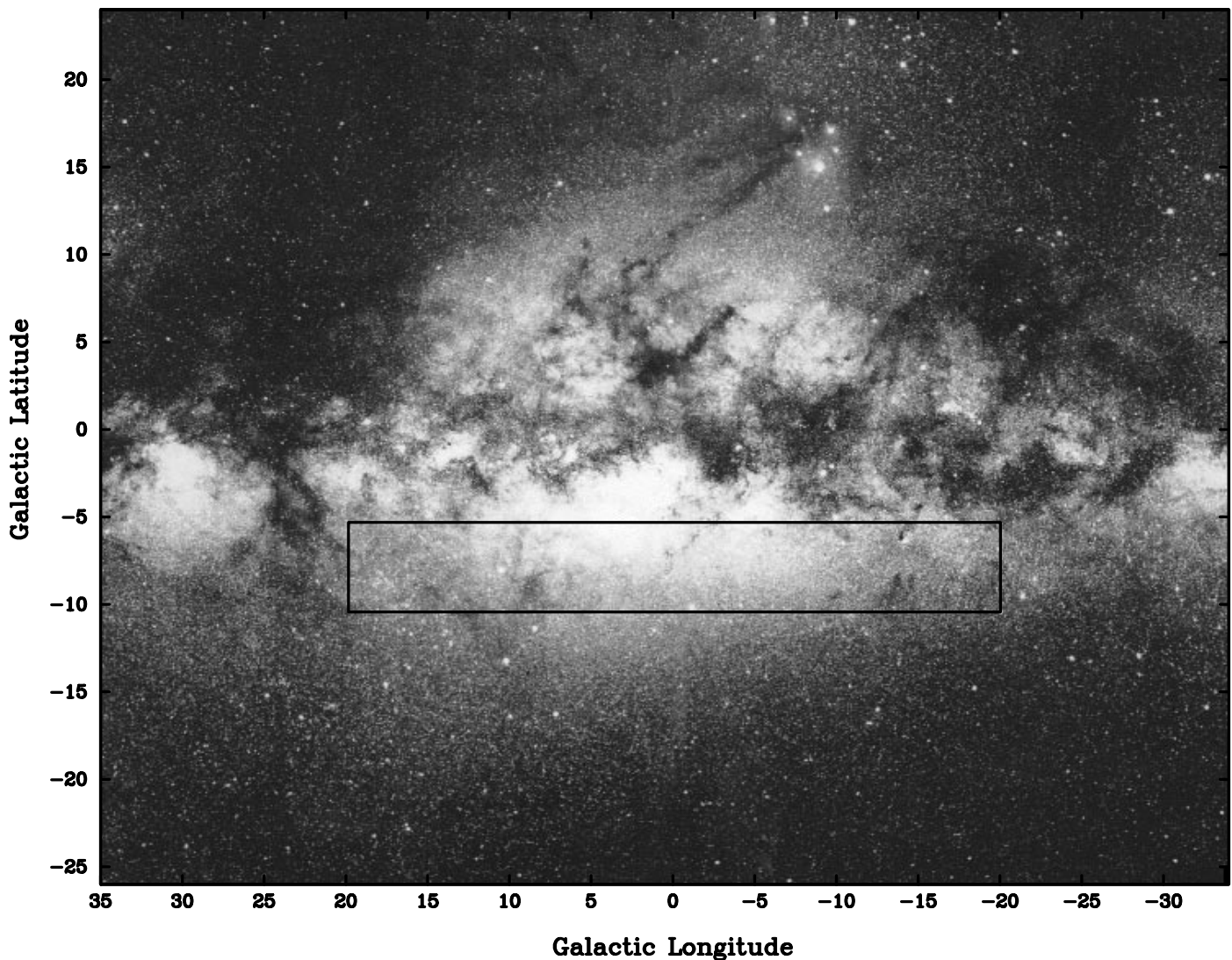


FIG. 1.—Image of the Galactic bulge taken by ESO. The field covers $\approx 70^\circ \times 50^\circ$.

the image. We did not use the dark frames, since no dark signal was detected. A minimum of three flat fields were taken by stepping the telescope slightly between each exposure and then combining them according to their wavelength band. For each band, a master flat was created, and the image was then divided by the master flat.

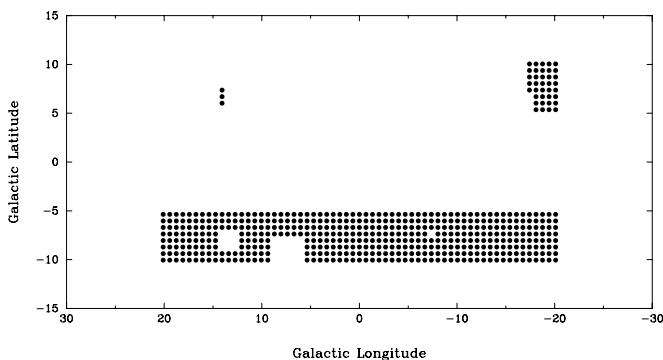


FIG. 2.—Optical Imaging Survey grid with fields observed

2.2. Search for Candidates

In studying the bulge of the Milky Way, we are challenged by the difficulty of finding faint and diffuse H α emitters in very dense star fields. The most straightforward method to detect our H α candidates was to combine the two H α frames and then *divide* the H α image by the continuum image for each field. With the correct scaling, the stars disappear in the quotient image, and the H α emitters are readily visible. The advantage of division over subtraction is that the noise in the quotient goes down where the signal goes up and the H α emitters appear. To illustrate this, say x and y are both normally distributed with $[\mu_x, \sigma_x]$ and $[\mu_y, \sigma_y]$ as their mean and standard deviation, respectively. Then, the mean of the ratio x/y is μ_x/μ_y , and its standard deviation is

$$\frac{\mu_x}{\mu_y} \sqrt{\frac{\sigma_x^2}{\mu_x^2} + \frac{\sigma_y^2}{\mu_y^2} - 2\rho \frac{\sigma_x \sigma_y}{\mu_x \mu_y}},$$

where ρ is the correlation coefficient between x and y (e.g., Menzel 1960). If we take the difference, the mean of $x-y$ is $\mu_x - \mu_y$, and its standard deviation is $(\sigma_x^2 + \sigma_y^2)^{1/2}$. In our

TABLE 3
OBSERVING LOG FOR THE 1.0 m OPTICAL IMAGING SURVEY

Date	Number of Nights	Clear Nights (%)	CCD Number
1993 May 25–31	7	65	11
1993 Jun 11–22	12	50	11
1993 Jul 19–29	11	30	4, 11
1993 Aug 9–18	10	55	4
1994 May 16–23	8	80	9
1994 May 31–Jun 5.....	6	60	6
1994 Jun 30–Jul 3.....	4	75	6
1994 Jul 7–12.....	6	30	6
1994 Aug 1–8.....	8	70	6

situation, where μ_x ($H\alpha$) $\approx \frac{1}{2}\mu_y$ (continuum) and (σ_x, σ_y) come from Poisson noise, the noise in the quotient goes like $(3/8\mu_x)^{1/2}$, while the noise in the difference goes like $(3\mu_x)^{1/2}$.

But a drawback of this procedure (the division) is that the photon statistics in the quotient image are no longer Gaussian. Since our goal here is to remove the stars and make the $H\alpha$ emitters appear for the purpose of detection, the photon statistics problem is not so important: we note here that we are not attempting photometry of the detected $H\alpha$ objects with this technique.

Combining two $H\alpha$ frames was necessary in order to remove cosmic rays. For the continuum, it was not crucial to obtain two frames, since the cosmic rays will appear as low (dark) values in the quotient image. Because the seeing varies during the night and from one night to another, we were careful to take the three images of a field during the same night and as close in time as possible.

Before dividing, we need to get the sky level and the total star signal similar in the three images, so we must perform two kind of adjustments.

1. A first scaling of the continuum image so that the total star signal above the sky is the same as for the $H\alpha$ image. This involve a multiplicative scaling.
2. An offset to adjust the sky level of the continuum image so that it is the same as for the $H\alpha$ image.

A division of the $H\alpha$ image by the scaled continuum image will then, in the absence of seeing effects and noise, cause the stars to disappear and leave behind only the $H\alpha$ emitters visible above the divided sky level. In principle, the pixel values of the quotient image will then lie near 1.0 except for $H\alpha$ absorption in some stars, (dark) cosmic rays from the continuum image, and the $H\alpha$ emitters.

We begin by registering the three images. Then we obtain the final $H\alpha$ image by combining the two $H\alpha$ images using a MINMAX reject algorithm in order to reject the highest value of each pixel: this allow for the rejection of cosmic rays. For a set of two images, the signal-to-noise ratio (S/N) of the MINMAX image is a factor of ≈ 1.2 higher than the S/N of a single image. The use of the MINMAX reject algorithm is also justified here by the fact that we do not intend to do any photometry, just to perform an object detection. Many of our nights were nonphotometric anyway.

In order to do the scaling to match the total star signal above the sky for the $H\alpha$ and the continuum images, we selected a box of Q pixels, carefully chosen to avoid bright saturated stars, bad columns, and vignetted regions. The total star signal in the box is $N_{\text{total}} - Qn_{\text{sky}}$, where N_{total} is

the total (stars plus sky) photon count in the box and n_{sky} is the mean pixel sky level in the box.

The sky level, n_{sky} , is the mode obtained from the pixel histogram, and N_{total} is derived directly. Thus the multiplicative factor, f , for the continuum image is $f = (N_{\text{total},\alpha} - Qn_{\text{sky},\alpha}) / (N_{\text{total},c} - Qn_{\text{sky},c})$.

After multiplying the continuum image by f , its total star signal is the same as for the $H\alpha$ image; i.e., the intensity scales for the continuum and $H\alpha$ images are now the same. The sky level of the continuum image is now $fn_{\text{sky},c}$. We wish to adjust the sky level of the continuum image to make it equal to the sky level of the $H\alpha$ image, so we then subtract from the scaled continuum image the constant $\Delta = fn_{\text{sky},c} - n_{\text{sky},\alpha}$ as the final step before dividing the $H\alpha$ image by the continuum image.

We now have the continuum image scaled and offset so that its total star signal above the sky and its sky level are the same as for the $H\alpha$ image. The last step toward finding $H\alpha$ -emitting objects is to divide the $H\alpha$ image by the scaled continuum image.

The resulting quotient image will then have pixel values near 1.0, except for the effects of the following:

1. $H\alpha$ -emitting objects. These appears as bright regions and are readily visible.
2. Cosmic rays in the continuum. These appears as regions of low signal in the quotient image.
3. Stars with strong $H\alpha$ absorption. These appear dark in the quotient image.
4. Residual misalignment, residual vignetting effects, errors in scaling, noncircular images resulting from bad tracking and telescope buffeting by high winds, bad focusing, and different seeing for the $H\alpha$ and continuum images. (We did not attempt to match the point spread function [PSF] for the $H\alpha$ and continuum images, because the PSFs are undersampled.)

The scaling procedure does not take $H\alpha$ absorption in individual stars into account. Therefore, the procedure is affected by the stellar population of the bright stars present in the field.

After a thorough and systematic visual examination of the quotient images for our 498 fields, we have a total of 148 $H\alpha$ detections. Figure 3 shows examples of images for a set of four objects. The montage is composed of the $H\alpha$, continuum, and quotient images. These four objects represent typical cases found in our fields. One of them, 345.26–08.8, is a catalogued planetary nebula. Object He 2–376 is catalogued as an emission-line star. The remaining two objects are new discoveries.

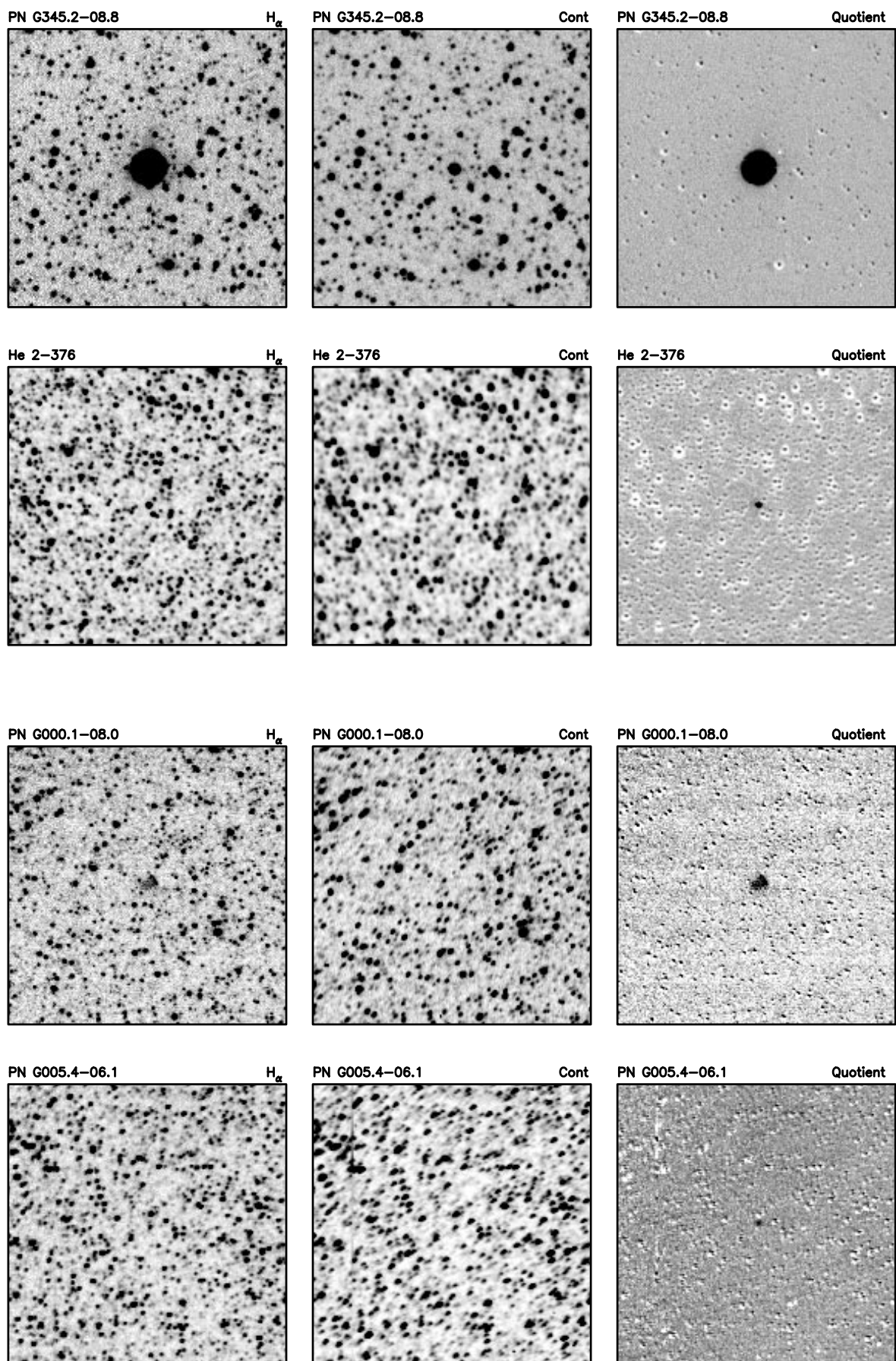


FIG. 3.—Montage of a set of four objects with the H_{α} , continuum, and quotient images

TABLE 4
SEARCH RESULTS OF THE 1.0 m OPTICAL IMAGING
SURVEY

Filter	Detections	Known	Candidates
H α	148	51	97
[O III].....	14	14	0

We did not use an automatic detection procedure, because it soon became clear that a visual search was very effective for identifying H α emitters and rejecting ghosts and defects.

The same technique was applied to the 15 [O III] fields. There was a total of 14 [O III] detections, all of which had been detected in H α . Two objects detected in the H α images were not detected in [O III]. Spectroscopy indicates that these two objects are symbiotic stars (symbiotic stars emit in H α and sometimes [O III], but the [O III] emission can be weak or absent).

2.3. Astrometry

The last step of the optical reduction is to perform an astrometric solution for each image containing a candidate in order to derive the equatorial and Galactic coordinates.

With about 10 Guide Star Catalogue (GSC) stars in each field, we used the Starlink astrometric program ASTROM to estimate (α, δ) and (l, b) for the PN candidates. The program uses a linear, six-coefficients fit to calculate the solution and gave root mean square (rms) residuals of less than 0.5 for the reference stars.

Once the equatorial coordinates are obtained for each candidate, the next step is to cross-check the position of our candidates with catalogs of known PNs in order to identify those that are already catalogued. We used the Acker et al. (1992) catalog, which is the most up-to-date. In addition, we searched through Ratag's and van de Steene's theses (Ratag 1990; van de Steene 1995), because, for Ratag's list of discoveries, if the optical finding chart was not available, Acker et al. (1992) listed their discoveries as "probable PNs" in their catalog; for van de Steene's list, her work came after the publication of the catalog.

Table 4 shows the result of the final count for our 148 detections in H α and 14 detections in [O III]. Of the 51 previously known objects, 45 are PNs and the remaining 6 are catalogued as either symbiotic stars or peculiar emission-line objects in the Acker et al. (1992) catalog. None of our objects was found in van de Steene's thesis, and objects found in Ratag's thesis were already reported in the catalog as "probable PNs."

We wished to ensure that all the Acker catalog objects have been recovered in our deep survey fields. We thus performed a search in the catalog within a radius of 15' of our field center (our circular field of view is roughly 30' in diameter). The search showed that seven objects from the catalog were not recovered in our fields. After investigating these objects, it became clear that they were all at the edge of our circular field of view and were lost in the vignetting of our frames (we recall that our grid of circular fields covers about half of the total area within the survey region).

3. THE 188 CENTIMETER SURVEY

Since PNs have strong emission lines, it is relatively quick and easy to measure their radial velocities spectro-

scopically. The Acker et al. (1992) catalog of Galactic PNs includes 326 objects located in the more extended bulge region of Galactic longitude, $l = \pm 30^\circ$ and Galactic latitude between $b = \pm(3.3$ and $15^\circ)$. Nearly half of these catalog objects lack any radial velocity measurements, and a fair number needed to be reobserved because of poor spectral resolution in the original measurements. We decided to make new velocity measures of this subsample in order to obtain a uniform quality sample. This is important, because we then know the error of the measurements, and, for many cases, we can reduce the velocity error.

3.1. Observations

Using the 188 cm (74 inch) telescope at Mount Stromlo Observatory, we obtained spectra for the 97 new H α objects detected in our 1.0 m telescope imaging survey and for 317 of the 326 PNs from the Acker catalog in the region $l = \pm 30^\circ$ and $b = \pm(3.3$ to $15^\circ)$.

We used the Boller and Chivens spectrograph with the 600 lines mm^{-1} grating blazed at 7500 Å in first order and the GEC 385 \times 578 UV coated CCD. The spectrograph slit width was 2". This CCD has a pixel size of 22.5 μm and a readout noise of 10. We binned the CCD with a factor 3 along the slit and a factor 1 in λ . The grating was set to have a wavelength coverage from 6200 to 6800 Å. A GG 475 filter in the beam was used to cut-off light from the second-order blue. This setup gave a wavelength scale of about 1 Å pixel^{-1} (50 km s^{-1}).

When possible, we took two spectra for each object in order to discriminate against cosmic rays and to determine our measurement error. Typical exposure times varied from 50 to 900 s. Each object spectrum was sandwiched between two comparison lamp (NeFe) exposures in order to provide a wavelength calibration.

In three observing seasons, we were allocated a total of 70 nights at the 188 cm telescope, 45% of which were clear. The observing log is summarized in Table 5 as follows: the period covered in each observing run (col. [1]), the number of nights run^{-1} (col. [2]), and the proportion of clear nights run^{-1} (col. [3]).

3.2. Data Reduction

The data reduction for the spectra is straightforward. We again used the IRAF environment to correct for electronic bias and illumination variation across the chip (Massey, Valdes, & Barnes 1992). We note, however, that the flat fields were obtained using a continuum lamp instead of twilight flat fields. Having removed the detector signature, we proceeded to correct the spectra for geometrical distor-

TABLE 5
OBSERVING LOG FOR THE 188 cm OPTICAL SPECTROSCOPY SURVEY

Date	Number of Nights	Clear Nights (%)
1993 Jun 18–25	8	40
1993 Jul 9–18	10	50
1994 Jun 6–13	8	40
1994 Jun 30–Jul 7	8	15
1995 May 2–7	6	30
1995 May 22–25	4	20
1995 Jun 22	1	100
1995 Jun 26–Jul 2	7	30
1995 Jul 31–Aug 7	8	55
1995 Aug 18–27	10	70

TABLE 6
SUMMARY OF THE CLASSIFICATION FOR THE
97 NEW CANDIDATES

Objects	Counts
PN	53
Probable PN	3
Symbiotic star	14
Probable symbiotic star	3
dMe	3
CV?	1
Spurious	20

tions, such as slit curvature and tilt, and then performed sky subtraction using two windows on each side of the PN spectrum. Throughout the correction procedure, we have used the *long-slit* package.

At this point, we are able to distinguish true or probable PNs from symbiotic stars on the criteria that a PN has narrow H α emission with possibly other emission lines from [N II] and [S II] and that a symbiotic star shows broad H α emission with possibly emission in He I. A few of our candidates turned out to be possible CVs or dMe stars. Table 6 summarizes the final count of our 97 new candidates as follows: the classification of objects (col. [1]) and the number of objects in each class (col. [2]).

3.3. Line Measurements

We measured the wavelength of the emission lines in order to obtain the mean radial velocity of each PN. The rest wavelengths (λ_0) of emission lines likely to be found in our wavelength window (from 6200–6800 Å) are shown in Table 7.

If more than one line was identified and measured for a given spectrum, we then applied a weight factor according to the strength of each line: $\langle V_r \rangle = \Sigma f_i v_{r,i} / \Sigma f_i$, where f_i is the flux of a line and $v_{r,i}$ its corresponding radial velocity. For PNs where we took two spectra, we then can calculate the mean velocity for each object from the two measurements. We determined our mean error to be 11 km s^{-1} .

As mentioned earlier, there were 193 catalog PNs with published radial velocities. Figure 4 show a comparison of our velocity values against the catalogued velocities. Apart from a few outliers, we find good agreement with the catalogued values.

3.4. IRAS Search

Several past surveys of PNs were performed using the ratios of the IRAS flux densities, F_{12}/F_{25} and F_{25}/F_{60} , in order to select a sample of PNs candidates with IRAS detection (Pottasch et al. 1988; Ratag 1990; van de Steene

TABLE 7
REST WAVELENGTH
VALUES OF
EMISSION LINES

Emission Line	λ_0 (Å)
[N II]	6548.1
H α	6562.7
[N II]	6583.4
[He I]	6678.4
[S II]	6716.4
[S II]	6730.8

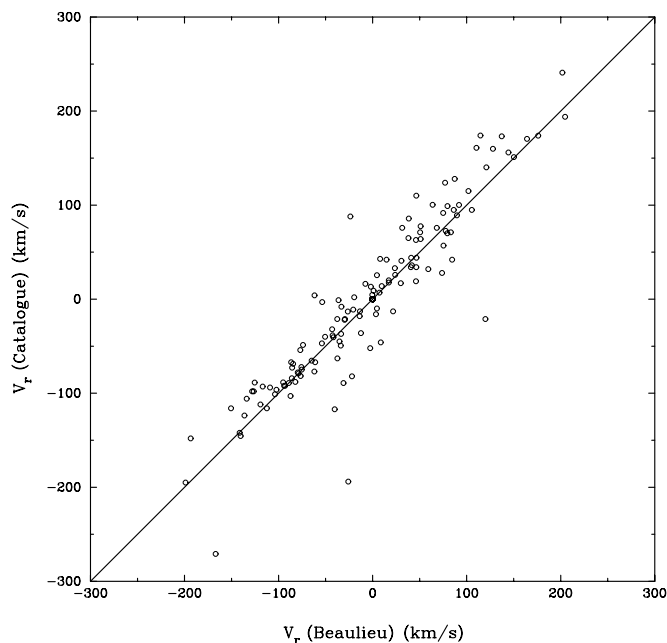


FIG. 4.—Comparison between the velocity values obtain from the 188 cm telescope and the catalogued values.

1995). It was shown that PNs seems to occupy a distinct region of $F_{12}/F_{25} \leq 0.35$ and $F_{25}/F_{60} \geq 0.3$ (note that the authors selected objects with flux qualities of 2 or 3, where 1 is the upper limit, 2 is moderate quality flux density, and 3 is good quality flux density). A considerable number of PNs were discovered using this selection criteria.

Using a search radius of $1'$, we thus performed a cross-check of our new PNs positions with the IRAS Point Source Catalog, Version 2 (1988; PSC) and found a match for 11 objects (see Table 8 for details of the flux quality for each object). Figure 5 shows an IRAS color-color plot of our 11 objects (regardless of their flux quality; *filled squares*) and the PNs from the Acker et al. (1992) catalog (*dots*) that have an IRAS detection with flux quality of 2 or 3 in F_{12} , F_{25} , and F_{60} . This yielded 323 objects from a total of 774 catalogued PNs having an IRAS entry. From our 11 objects, only two have flux quality of 2 or 3. For the nine objects having one or more flux quality of 1, we drew an arrow for each upper limit to illustrate where the object would be shifted on the color-color plot if their flux quality had been better. We have two PNs with upper limits on both F_{25} and F_{60} . For those two, we cannot tell which way the horizontal arrow should go; therefore we drew two broken horizontal arrows in each direction.

In Figure 5, we have also overplotted different regions that indicate the kind of objects most likely to be found in an IRAS color-color diagram in the same fashion as van de Steene (1995). Relatively few of our new PNs are seen at IRAS wavelengths, and those that were seen have colors that would not have led to their selection as PN candidates. For six of the PNs, an improved flux quality might bring them back to the PNs region. But for five PNs, their colors are too far from the PNs region.

This is quite unexpected. The reason for most of these new objects to lie so far away from the PNs region is not clear. These objects include a mixture of compact and extended PNs, and there is no evidence for any correlation between their IRAS color, angular diameter, and position

TABLE 8
NEWLY DISCOVERED PNs

Object	PN G (<i>lll.l ± bb.b</i>)	α (J2000)	δ (J2000)	Comments	V_r (helio) (km s ⁻¹)	$v_1 - v_2$ (km s ⁻¹)	IRAS Source	F_{12} (Jy)	F_{25} (Jy)	F_{60} (Jy)	F_{100} (Jy)	$F_{Quality}$
SB1	000.1 - 08.0	18 18 48.4	-32 47 56.5	PN	-54	-5
SB2	000.5 - 05.3	18 08 34.7	-31 06 52.1	PN	3	0
SB3	000.7 - 06.1	18 12 14.4	-31 19 58.9	PN	68	0
SB4	001.1 - 06.4	18 14 14.1	-31 11 09.2	PN	21	-8
SB5	001.3 - 05.6	18 11 15.2	-30 37 48.9	PN	-31	6
SB6	001.6 - 05.9	18 13 15.5	-30 26 04.6	PN	31	2
SB7	003.3 - 06.1	18 17 46.1	-29 06 04.9	PN	-27	-2
SB8	004.2 - 05.2	18 15 50.3	-27 48 59.7	PN	40	-5
SB9	004.6 - 09.9	18 35 42.4	-29 38 22.2	PN	-22
SB10	004.7 - 05.5	18 18 06.9	-27 31 35.4	PN	54
SB11	005.2 - 05.9	18 20 44.7	-27 15 48.0	PN	95	-20	172497	4.8	2.9	0.7	4.1	3321
SB12	005.4 - 06.1	18 21 55.1	-27 09 46.2	PN	25
SB13	006.5 - 05.8	18 23 00.0	-26 05 17.1	PN probable	57	27
SB14	007.7 - 05.3	18 23 42.4	-24 47 26.2	PN	31
SB15	009.3 - 06.5	18 31 14.7	-23 58 03.2	PN probable	165	4
SB16	009.4 - 05.6	18 28 21.1	-23 25 28.0	PN	61	8
SB17	011.1 - 07.9	18 40 19.9	-22 54 29.9	PN (V 348 Sgr)	145	...	181973	5.5	3.0	2.9	13.4	3331
SB18	011.4 - 07.3	18 38 43.3	-22 24 15.0	PN	-2	30
SB19	014.4 - 06.1	18 39 39.9	-19 14 12.5	PN	72	...	181710	0.3	0.5	1.4	26.7	1331
SB20	014.8 - 08.4	18 49 24.3	-19 52 15.6	PN	-24	4
SB21	016.0 - 07.6	18 48 11.4	-18 29 39.8	PN	66	...	185736	0.3	0.5	0.7	15.1	1331
SB22	016.7 - 07.3	18 48 30.5	-17 43 56.5	PN	-10
SB23	017.5 - 07.4	18 50 13.7	-17 02 27.6	PN	52	4
SB24	017.5 - 09.2	18 57 16.6	-17 50 49.1	PN	22
SB25	341.0 + 09.4	16 13 38.1	-37 59 57.9	PN	-93	13
SB26	341.7 - 06.0	17 21 02.8	-47 35 25.8	PN	-154	-25
SB27	341.9 + 08.8	16 19 13.9	-37 47 30.5	PN probable	-2	-8
SB28	342.3 - 06.0	17 22 52.5	-47 02 45.3	PN	-27	...	145844	0.4	0.3	0.7	29.9	3111
SB29	343.7 - 09.6	17 45 33.4	-47 43 49.7	PN	-88	-5	155474	3.4	2.9	0.7	2.3	3311
SB30	343.9 - 05.8	17 27 02.2	-45 32 39.7	PN	67	9
SB31	347.9 - 06.0	17 40 03.5	-42 24 02.6	PN	-70	23	153025	0.3	0.9	1.1	24.9	1331
SB32	349.7 - 09.1	17 59 26.9	-42 24 52.3	PN	186
SB33	351.2 - 06.3	17 50 27.7	-39 40 17.3	PN	-58	24
SB34	351.5 - 06.5	17 52 09.6	-39 32 16.0	PN	-57	-3	158612	0.3	0.8	2.4	18.1	1331
SB35	351.7 - 06.6	17 53 02.7	-39 24 08.8	PN	-120	-8
SB36	352.0 - 06.7	17 54 20.6	-39 10 39.8	PN	35	-13
SB37	352.6 - 04.9	17 47 52.7	-37 48 03.4	PN	20	...	156740	0.3	0.7	1.1	9.1	1311
SB38	352.7 - 08.4	18 03 28.9	-39 21 26.8	PN	59	4
SB39	353.3 - 08.3	18 04 31.8	-38 47 36.8	PN	6
SB40	354.7 - 07.2	18 02 55.6	-37 08 15.3	PN	-69	-2
SB41	354.7 - 10.0	18 15 39.1	-38 27 56.4	PN	34	-1
SB42	355.3 - 07.5	18 05 52.5	-36 45 35.9	PN	40	52
SB43	355.8 - 08.7	18 12 23.7	-36 52 50.9	PN	-74	-4
SB44	356.0 - 07.4A	18 07 07.6	-36 02 52.8	PN	1	3	165874	0.5	0.4	0.5	3.6	3111
SB45	356.0 - 07.4B	18 06 52.2	-36 06 41.2	PN	-116	2
SB46	356.1 - 08.6	18 12 39.7	-36 31 51.3	PN	54	2
SB47	356.3 - 07.3	18 07 21.3	-35 45 43.8	PN	-27	0
SB48	356.4 - 06.8	18 05 14.3	-35 28 07.4	PN	10	-2
SB49	357.2 - 09.8	18 20 09.4	-36 07 25.3	PN	20	-10
SB50	357.3 - 06.5	18 06 08.2	-34 33 31.1	PN	0	35
SB51	357.4 - 07.2	18 09 16.1	-34 47 41.0	PN	-222	-14
SB52	358.3 - 07.3	18 11 39.9	-34 00 22.6	PN	-49	-16
SB53	358.7 - 05.1	18 03 28.4	-32 37 25.6	PN	-14	-6
SB54	359.3 - 06.0	18 08 31.3	-32 29 54.4	PN	38
SB55	359.4 - 08.5	18 19 26.4	-33 37 07.5	PN	163	...	171836	0.3	0.5	0.8	10.3	1331
SB56	359.9 - 07.4	18 15 32.4	-32 38 01.5	PN	222	-31

NOTE.—Units of right ascension are hours, minutes, and seconds, and units of declination are degrees, arcminutes, and arcseconds.

on the longitude-velocity diagram. One possibility is contamination of background galaxies and stars in the large beam of the *IRAS* survey. Our objects are in crowded fields, and it is possible that their fluxes are contaminated by asymptotic giant branch stars and background galaxies.

3.5. Summary of the Results

Table 8 lists our new PNs. Column (1) gives the name of the new PN; column (2) gives the (*l*, *b*) coordinates; columns (3, 4) give the (α , δ) coordinates in J2000.0; column

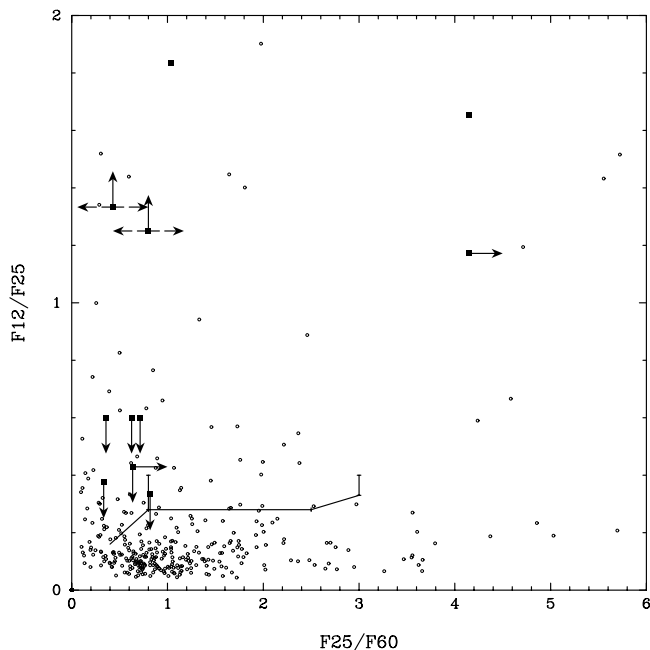


FIG. 5.—Newly discovered PNs, which have a match in the *IRAS/PS* catalog, overlaid on a color-color diagram of catalogued PNs. Our 11 matches are the filled squares.

(5) gives comments for each PN; column (6) gives the mean radial velocity corrected for heliocentric motion; column (7) gives the difference in velocities between our two spectra when two were available; column (8) gives the *IRAS* detection number from the PSC (when applicable); columns (9), (10), (11), and (12) give the far-IR flux density at 12, 25, 60, and 100 μm in Jy, respectively; and column (13) gives the *IRAS* flux quality, where 1 is the upper limit, 2 is moderate quality, and 3 is good quality.

Table 9 contains our velocity data for the 317 PNs from the Acker catalog. Column (1) gives the name of the PN, column (2) gives the heliocentric radial velocity value reported in the catalog, column (3) gives our mean heliocentric radial velocity value, and column (4) gives the velocity difference between our two spectra when two were available.

4. THE 2.3 METER OBSERVATIONS

In 1995 June and 1996 July, our new PNs were reobserved using the 2.3 m telescope of Siding Spring Observatory in order to obtain higher resolution photometric data.

The focal-reducing imager at the Nasmyth B focus was used with a Tek 1024 CCD. The $H\alpha$ filter is a Bausch and Lomb three-cycle, 90 mm diameter interference filter ($\lambda_{\text{peak}} = 6586 \text{ \AA}$ and $\text{FWHM} = 16 \text{ \AA}$) and was tilted at an angle of 7° in order to obtain the central wavelength for $H\alpha$ $\lambda 6563$. This filter was designed to transmit $H\alpha$ at the normal incidence and reject $[\text{N II}]$ at better than the 1% level. The $[\text{N II}]$ leakage of this filter, even in the tilted position and in the $f/8$ beam, is less than 5%.

In Figure 6, we present the atlas of our new PNs using the 2.3 m data, which offers much better quality images. Each page is a montage of six newly found PNs with the $H\alpha$ (*upper image*) and the continuum (*lower image*) as a pair. North is up, and east at the left. Most objects are centered (or nearly centered) in the image and are identified by thick

TABLE 9
NEW RADIAL VELOCITIES OF ACKER CATALOG

PN G (<i>lll.l</i> \pm <i>bb.b</i>)	$V_r(\text{catalog})$ (km s^{-1})	$V_r(\text{helio})$ (km s^{-1})	$v_1 - v_2$
000.0 - 06.8.....	-84	-86	...
000.1 - 05.6.....	...	-70	-4
000.2 - 04.6.....	...	117	-17
000.3 - 04.6.....	-17	-29	...
000.3 + 06.9.....	-46	9	...
000.3 + 12.2.....	-33	-36	...
000.7 - 03.7.....	-54	-77	-5
000.7 + 04.7.....	...	40	-5
000.7 - 07.4.....	-21	-30	...
000.8 - 07.6.....	...	33	-9
000.9 - 04.8.....	-156	-155	-4
001.2 - 03.9.....	...	-92	31
001.4 - 03.4.....	-117	-40	9
001.4 + 05.3.....	36	42	...
001.5 - 06.7.....	-19	-12	...
001.7 - 04.4.....	-52	-3	7
001.7 - 04.6.....	-106	-134	...
001.7 + 05.7.....	34	40	...
001.8 - 03.8.....	...	-222	13
002.0 - 06.2.....	-112	-119	...
002.0 - 13.4.....	19	22	3
002.1 - 04.2.....	-116	-151	-14
002.2 - 06.3.....	-1	-36	...
002.2 - 09.4.....	-30	-44	...
002.3 - 03.4.....	...	-158	-1
002.3 - 07.8.....	-82	-22	...
002.4 - 03.7.....	-70	-92	-4
002.4 + 05.8.....	-101	-104	...
002.5 - 05.4.....	107	90	...
002.6 - 03.4.....	241	202	25
002.6 + 04.2.....	...	-174	1
002.6 + 08.1.....	2	-20	17
002.7 - 04.8.....	-92	-93	...
002.9 - 03.9.....	...	33	-19
002.9 + 06.5.....	...	70	6
003.1 + 03.4.....	87	80	6
003.2 - 04.4.....	124	77	2
003.2 - 06.2.....	100	64	...
003.3 - 04.6.....	152	157	-19
003.3 - 07.5.....	32	59	-2
003.4 - 04.8.....	-21	120	...
003.5 - 04.6.....	-20	-3	...
003.7 - 04.6.....	174	115	...
003.7 + 07.9.....	...	41	-27
003.8 + 05.3.....	-59	-88	...
003.9 - 14.9.....	-65	-65	...
004.0 - 05.8.....	...	159	-32
004.0 - 11.1.....	50	39	...
004.1 - 03.8.....	-63	-38	-1
004.2 - 04.3.....	...	-5	3
004.2 - 05.9.....	57	75	...
004.5 + 06.8.....	...	-180	-25
004.6 + 06.0.....	160	151	...
004.7 - 11.8.....	...	115	7
004.8 - 05.0.....	-10	5	21
004.9 + 04.9.....	26	24	...
004.9 - 04.9.....	-75	-107	...
005.0 - 03.9.....	...	-122	-3
005.0 + 04.4.....	17	30	8
005.1 - 08.9.....	...	56	3
005.2 + 04.2.....	...	132	-6
005.2 + 05.6.....	18	17	...
005.5 - 04.0.....	...	-53	-5
005.6 - 04.7.....	17	53	10
005.7 - 03.6.....	...	-91	8

TABLE 9—Continued

PN G ($ll.l \pm bb.b$)	V_r (catalog) (km s^{-1})	V_r (helio) (km s^{-1})	$v_1 - v_2$
005.7 - 05.3.....	-72	-76	...
005.8 + 05.1.....	-56	-62	...
005.8 - 06.1.....	73	78	...
006.0 - 03.6.....	157	136	12
006.1 + 08.3.....	92	75	...
006.2 - 03.7.....	123	118	-2
006.3 + 04.4.....	-116	-113	-3
006.4 - 04.6.....	...	47	31
006.8 - 03.4.....	...	89	9
006.8 + 04.1.....	100	92	6
006.8 - 08.6.....	...	72	-37
007.0 - 06.0.....	42	85	...
007.0 + 06.3.....	-7	-26	...
007.0 - 06.8.....	115	102	...
007.5 + 04.3.....	-108	-134	2
007.5 + 07.4.....	13	-2	...
007.6 + 06.9.....	-65	-66	...
007.8 - 03.7.....	70	79	2
007.8 - 04.4.....	161	110	11
007.9 + 10.1.....	...	-45	55
008.0 + 03.9.....	16	-8	-7
008.1 - 04.7.....	71	83	...
008.2 - 04.8.....	157	119	...
008.2 + 06.8.....	...	23	10
008.3 - 07.3.....	194	205	...
008.4 - 03.6.....	84	70	3
008.6 - 07.0.....	...	26	3
008.8 + 05.2.....	44	47	...
009.0 + 04.1.....	-18	-32	1
009.3 + 04.1.....	...	16	-4
009.4 - 05.0.....	14	10	...
009.4 - 09.8.....	46	50	...
009.6 + 10.5.....	...	30	-31
009.6 - 10.6.....	174	176	...
009.6 + 14.8.....	-48	-40	...
009.8 - 04.6.....	-13	22	...
010.4 + 04.5.....	-21	-46	7
010.7 - 06.4.....	-145	-141	...
010.7 - 06.7.....	...	-84	-3
010.7 + 07.4.....	...	116	-20
011.0 - 05.1.....	-72	-69	...
011.0 + 05.8.....	-94	-109	...
011.0 + 06.2.....	4	-33	...
011.1 + 07.0.....	...	-81	31
011.1 + 11.5.....	86	38	...
011.3 - 09.4.....	-21	3	...
011.7 - 06.6.....	-22	-30	7
011.9 + 04.2.....	-73	-86	-9
012.2 + 04.9.....	...	43	7
012.5 - 09.8.....	34	41	...
013.0 - 04.3.....	...	81	24
013.1 + 04.1.....	-37	-60	-24
013.4 - 03.9.....	140	121	3
013.7 - 10.6.....	...	37	3
013.8 - 07.9.....	...	42	13
014.0 - 05.5.....	...	-42	16
014.2 - 07.3.....	-89	-95	...
014.3 - 05.5.....	...	-29	25
014.6 - 04.3.....	27	5	3
014.7 - 11.8.....	...	20	...
014.9 + 06.4.....	...	-5	...
015.4 - 04.5.....	63	46	2
015.9 + 03.3.....	128	87	11
016.0 - 04.3.....	-41	-42	-2
016.0 + 13.5.....	...	10	-3
016.1 - 04.7.....	88	-24	...

TABLE 9—Continued

PN G ($ll.l \pm bb.b$)	V_r (catalog) (km s^{-1})	V_r (helio) (km s^{-1})	$v_1 - v_2$
017.6 - 10.2.....	23	3	...
017.9 - 04.8.....	71	51	...
018.9 + 03.6.....	28	31	-2
018.9 + 04.1.....	-16	4	-5
019.4 - 05.3.....	41	31	...
019.4 - 13.6.....	...	-37	-13
019.7 - 04.5.....	76	88	...
019.8 + 05.6.....	...	86	4
020.7 - 05.9.....	...	46	-7
021.1 - 05.9.....	26	5	-2
021.2 - 03.9.....	...	-11	-1
022.5 + 04.8.....	...	24	-3
023.0 + 04.3.....	...	119	16
023.3 - 07.6.....	...	54	-41
024.1 + 03.8.....	89	90	-1
024.2 - 05.2.....	19	46	4
024.2 + 05.9.....	-21	-38	1
024.3 - 03.3.....	...	1	-10
025.0 - 11.6.....	...	-10	...
025.3 - 04.6.....	...	-85	15
025.4 - 04.7.....	-36	-13	2
025.9 - 10.9.....	...	96	-2
027.3 - 03.4.....	...	28	-5
027.4 - 03.5.....	110	47	9
027.6 + 04.2.....	95	105	58
027.6 - 09.6.....	151	150	-1
028.0 + 10.2.....	...	49	-10
028.2 - 04.0.....	...	65	11
028.5 + 05.1.....	42	15	10
028.7 - 03.9.....	...	-20	7
029.2 - 05.9.....	-39	-43	-1
029.8 - 07.8.....	...	89	-4
330.2 + 05.9.....	...	-33	-3
330.6 - 03.6.....	-89	-89	3
330.7 + 04.1.....	...	-9	6
330.9 + 04.3.....	...	27	0
331.1 - 05.7.....	...	-52	-74
331.4 - 03.5.....	33	24	-18
331.5 - 03.9.....	-18	-14	0
332.0 - 03.3.....	-77	-62	8
332.3 - 04.2.....	64	51	6
332.9 - 09.9.....	...	-67	1
333.4 - 04.0.....	...	-88	11
334.3 - 09.3.....	44	41	0
334.8 - 07.4.....	...	-77	-7
335.2 - 03.6.....	...	-97	9
335.4 + 09.2.....	...	-62	4
335.6 - 04.0.....	...	24	-7
335.9 - 03.6.....	...	-85	-2
336.2 - 06.9.....	-49	-34	-5
336.3 - 05.6.....	-67	-87	4
336.8 - 07.2.....	...	8	-3
336.9 + 08.3.....	...	-159	0
336.9 - 11.5.....	...	-14	...
337.4 - 09.1.....	...	-101	-2
337.5 - 05.1.....	...	52	3
337.6 - 04.2.....	...	-96	0
338.1 - 08.3.....	9	1	...
338.8 + 05.6.....	-27	-61	-9
340.4 - 14.1.....	...	-279	-16
340.8 + 10.8.....	...	9	21
340.8 + 12.3.....	...	-79	22
340.9 - 04.6.....	...	-2	-9
341.5 - 09.1.....	...	-25	-17
341.6 + 13.7.....	-103	-87	...
341.8 + 05.4.....	37	36	...

TABLE 9—Continued

PN G (<i>lll.l ± bb.b</i>)	V_r (catalog) (km s ⁻¹)	V_r (helio) (km s ⁻¹)	$v_1 - v_2$
342.1 + 10.8.....	7	7	...
342.5 - 14.3.....	46	43	...
342.8 - 06.6.....	-88	-82	...
342.9 - 04.9.....	-38	-19	...
343.4 + 11.9.....	...	67	-17
343.5 - 07.8.....	...	-142	-7
343.6 + 03.7.....	-194	-26	-14
344.2 + 04.7.....	-142	-142	9
344.4 - 06.1.....	...	-35	3
344.8 + 03.4.....	...	-131	-4
345.0 + 03.4.....	...	32	0
345.0 + 04.3.....	...	15	-17
345.0 - 04.9.....	-78	-80	...
345.2 - 08.8.....	-83	-94	...
345.3 - 10.2.....	...	21	-16
345.5 + 15.1.....	...	-19	6
345.6 + 06.7.....	-32	-43	...
346.0 + 08.5.....	-83	-93	...
346.2 - 08.2.....	-49	-74	...
346.3 - 06.8.....	35	17	...
346.9 + 12.4.....	-13	-14	...
347.4 + 05.8.....	-102	-101	-14
348.0 + 06.3.....	...	-52	-5
348.0 - 13.8.....	-124	-136	...
348.4 - 04.1.....	...	-208	-16
348.8 - 09.0.....	...	-53	-19
349.2 - 03.5.....	...	-12	-2
349.3 - 04.2.....	...	13	2
349.8 + 04.4.....	-184	-186	0
350.1 - 03.9.....	-37	-34	-5
350.5 - 05.0.....	-45	-35	...
350.9 + 04.4.....	-20	-25	14
351.0 - 10.4.....	...	-38	0
351.1 + 04.8.....	-40	-51	37
351.2 + 05.2.....	-98	-128	...
351.3 + 07.6.....	...	8	-10
351.6 - 06.2.....	-16	-28	...
351.7 - 10.9.....	...	-58	24
351.9 + 09.0.....	...	-74	10
352.0 - 04.6.....	-8	-33	...
352.1 + 05.1.....	27	26	...
352.9 - 07.5.....	5	0	-9
352.9 + 11.4.....	...	-2	-16
353.2 - 05.2.....	...	-151	1
353.3 + 06.3.....	-89	-126	...
353.7 + 06.3.....	-56	-56	...
353.7 - 12.8.....	...	-50	-9
354.2 + 04.3.....	-75	-75	-5
354.4 - 07.8.....	...	-124	0
354.5 + 03.3.....	...	-165	4
354.9 + 03.5.....	...	-72	19
355.1 - 06.9.....	-69	-85	-9
355.4 - 04.0.....	...	-84	-10
355.7 - 03.4.....	...	38	10
355.7 - 03.5.....	160	128	8
355.9 + 03.6.....	-148	-193	-13
355.9 - 04.2.....	-98	-127	-5
356.1 - 03.3.....	...	-165	-7
356.2 - 04.4.....	-271	-167	13
356.3 - 06.2.....	-47	-54	...
356.5 - 03.6.....	...	-37	-2
356.5 - 03.9.....	-50	-117	-8
356.5 + 05.1.....	...	-48	-19
356.6 - 07.8.....	...	-19	10
356.7 - 04.8.....	76	68	...
356.7 - 06.4.....	...	-206	-5

TABLE 9—Continued

PN G (<i>lll.l ± bb.b</i>)	V_r (catalog) (km s ⁻¹)	V_r (helio) (km s ⁻¹)	$v_1 - v_2$
356.8 + 03.3.....	330	168	0
356.8 - 05.4.....	-195	-199	...
356.8 - 11.7.....	...	-60	-6
356.9 + 04.4.....	-156	-170	-10
356.9 + 04.5.....	78	51	2
356.9 - 05.8.....	173	137	...
357.1 + 03.6.....	-191	-208	-8
357.1 + 04.4.....	...	52	-1
357.1 - 04.7.....	76	31	...
357.1 - 06.1.....	24	11	...
357.2 - 04.5.....	-79	-79	7
357.2 + 07.4.....	156	144	...
357.3 + 03.3.....	-69	-132	...
357.3 + 04.0.....	...	76	-16
357.4 - 03.5.....	-3	-54	9
357.4 - 04.6.....	-92	-94	...
357.6 - 03.3.....	...	114	2
357.9 - 03.8.....	...	-32	1
357.9 - 05.1.....	2	-5	...
358.0 - 05.1.....	...	-132	-7
358.0 + 07.5.....	43	8	...
358.0 + 09.3.....	...	-8	0
358.2 + 03.5.....	50	51	-16
358.2 + 03.6.....	-96	-102	5
358.2 + 04.2.....	95	86	-4
358.4 + 03.3.....	...	122	...
358.5 + 03.7.....	...	-168	-1
358.5 - 04.2.....	-13	-26	18
358.5 + 05.4.....	4	-62	...
358.5 - 07.3.....	-30	-30	...
358.6 - 05.5.....	34	46	...
358.6 + 07.8.....	12	6	...
358.7 - 05.2.....	28	74	...
358.7 + 05.2.....	37	45	...
358.8 + 04.0.....	...	33	8
358.8 + 04.1.....	...	46	12
358.9 + 03.4.....	65	38	5
358.9 - 03.7.....	99	80	10
359.0 - 04.1.....	-11	-21	3
359.0 - 04.8.....	20	17	...
359.1 + 15.1.....	...	2	-5
359.2 + 04.7.....	...	-237	42
359.3 + 03.6.....	...	-49	-5
359.4 - 03.4.....	...	107	-12
359.6 - 04.8.....	...	-108	6
359.7 - 04.4.....	200	213	...
359.8 + 03.7.....	-93	-117	17
359.8 + 05.2.....	-89	-31	...
359.8 + 05.6.....	73	76	...
359.8 + 06.9.....	-67	-61	...
359.8 - 07.2.....	-49	-74	...
359.9 - 04.5.....	170	164	2
359.9 + 05.1.....	-82	-77	...
359.9 - 05.4.....	-19	19	...

lines on the sides. Each image is 272×272 pixels on a side with $0''.6$ pixel⁻¹. The newly found PNs are ordered by increasing galactic number and are identified following the designation system, PN G *lll.l ± bb.b*, which has been adopted by Acker et al. (1992).

4.1. H α Fluxes

In order to obtain the total H α flux for each PN, we proceeded with the same technique used in § 2.2 except for the last step: we matched the PSF of both the H α and the

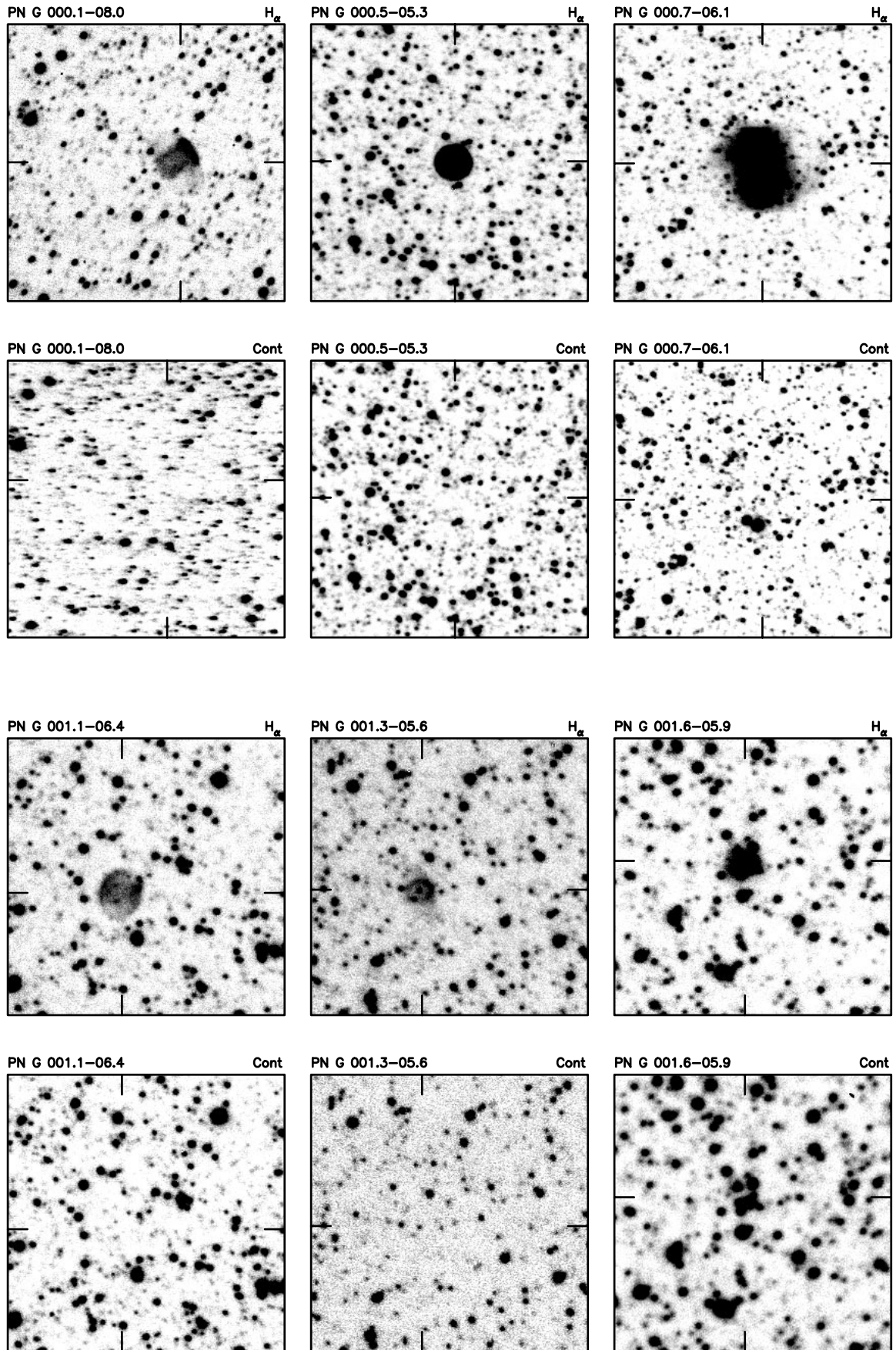


FIG. 6a

FIG. 6.—Atlas of the 56 new PNs. The H α (upper panels) and continuum (lower panels) images are presented. North is up and east at the left.

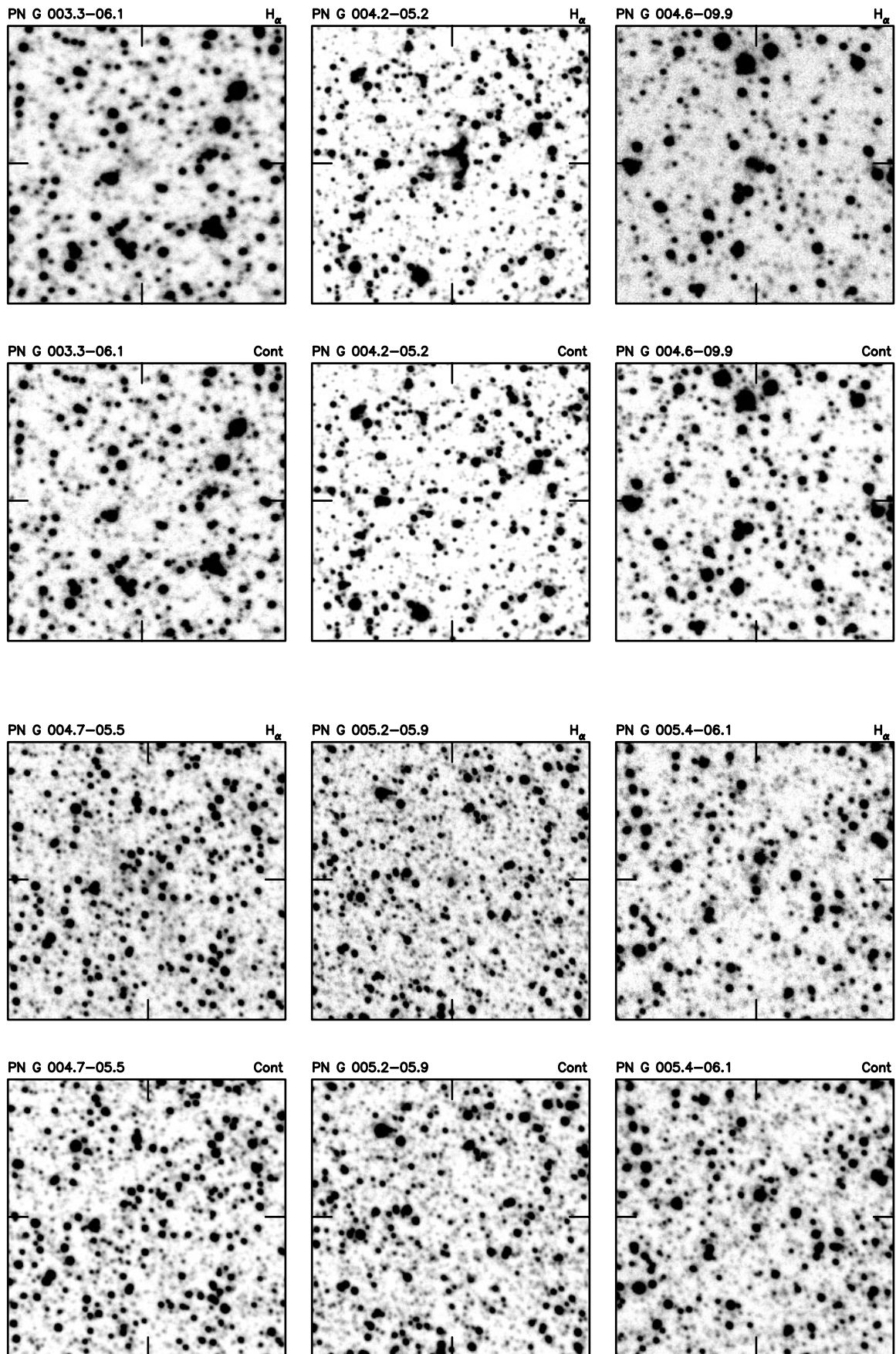


FIG. 6b

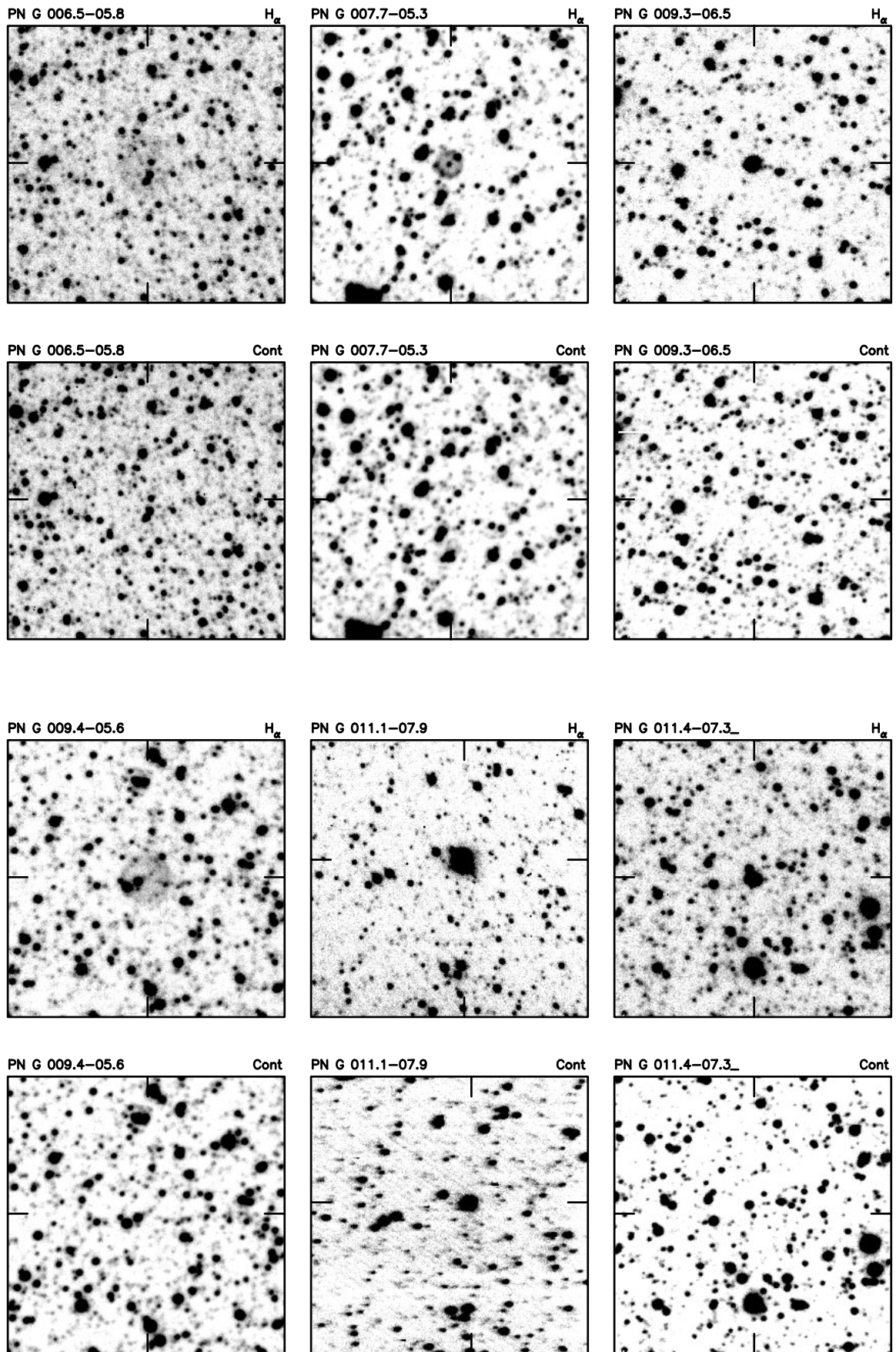


FIG. 6c

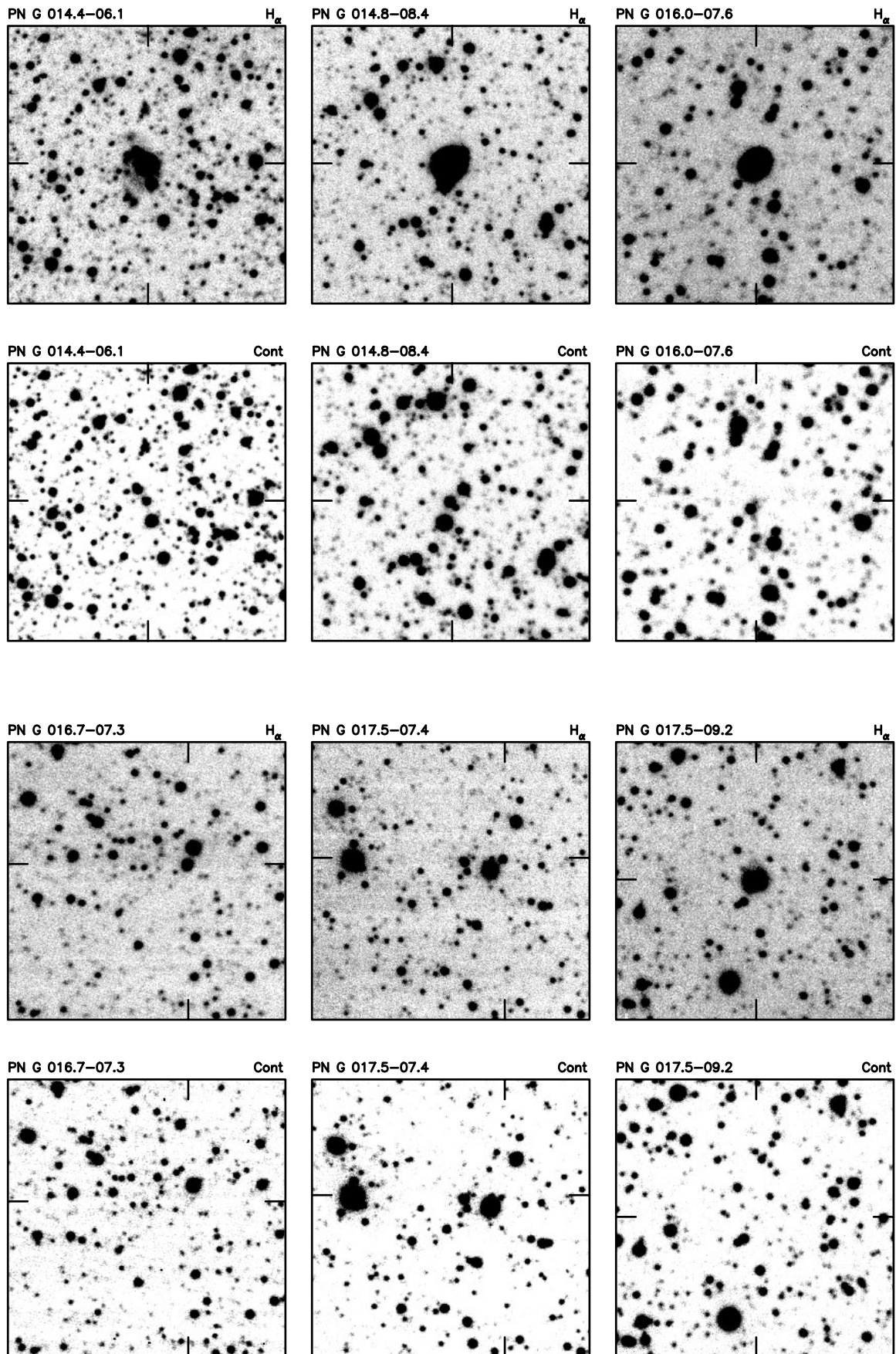


FIG. 6d

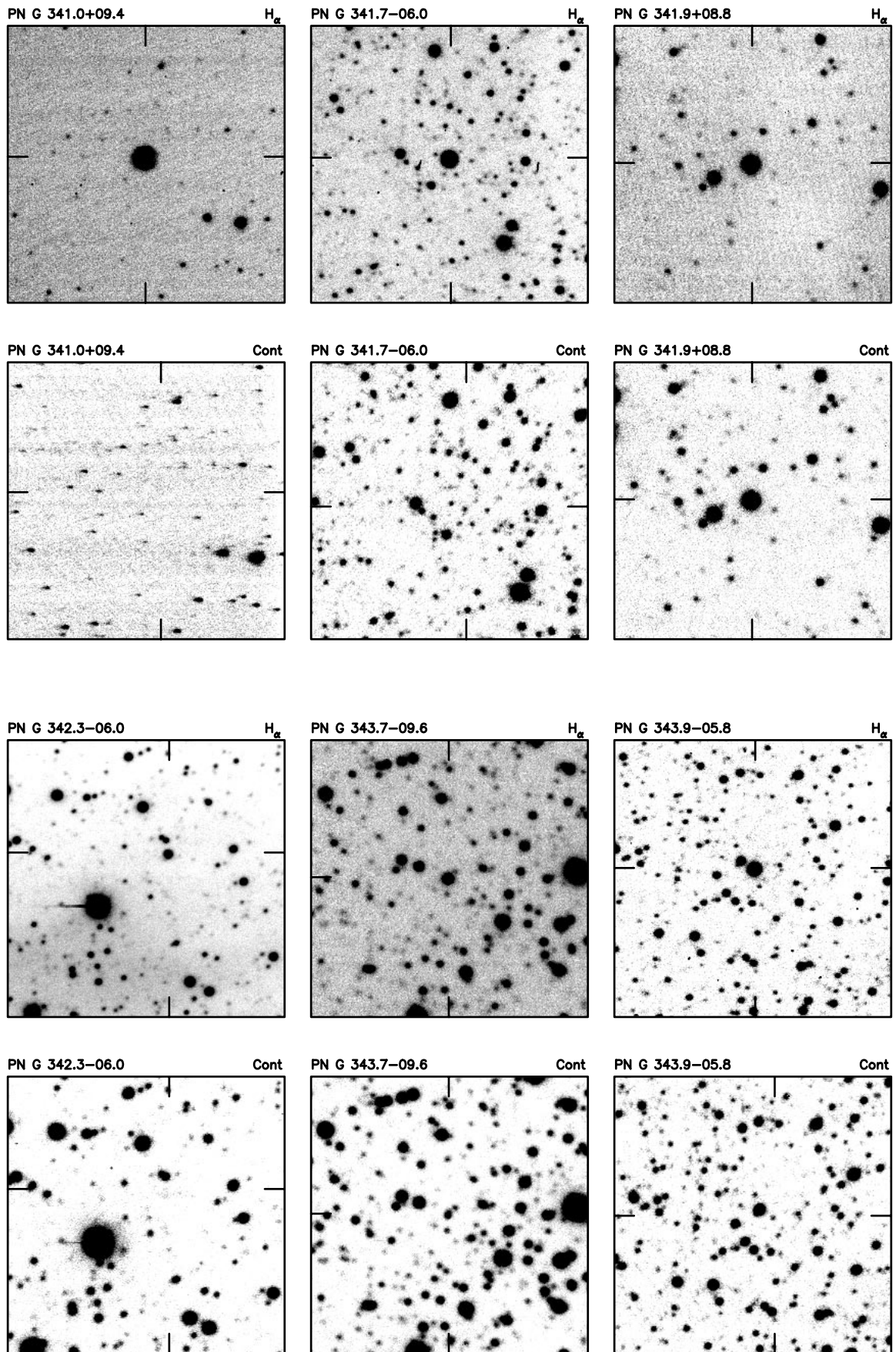


FIG. 6e

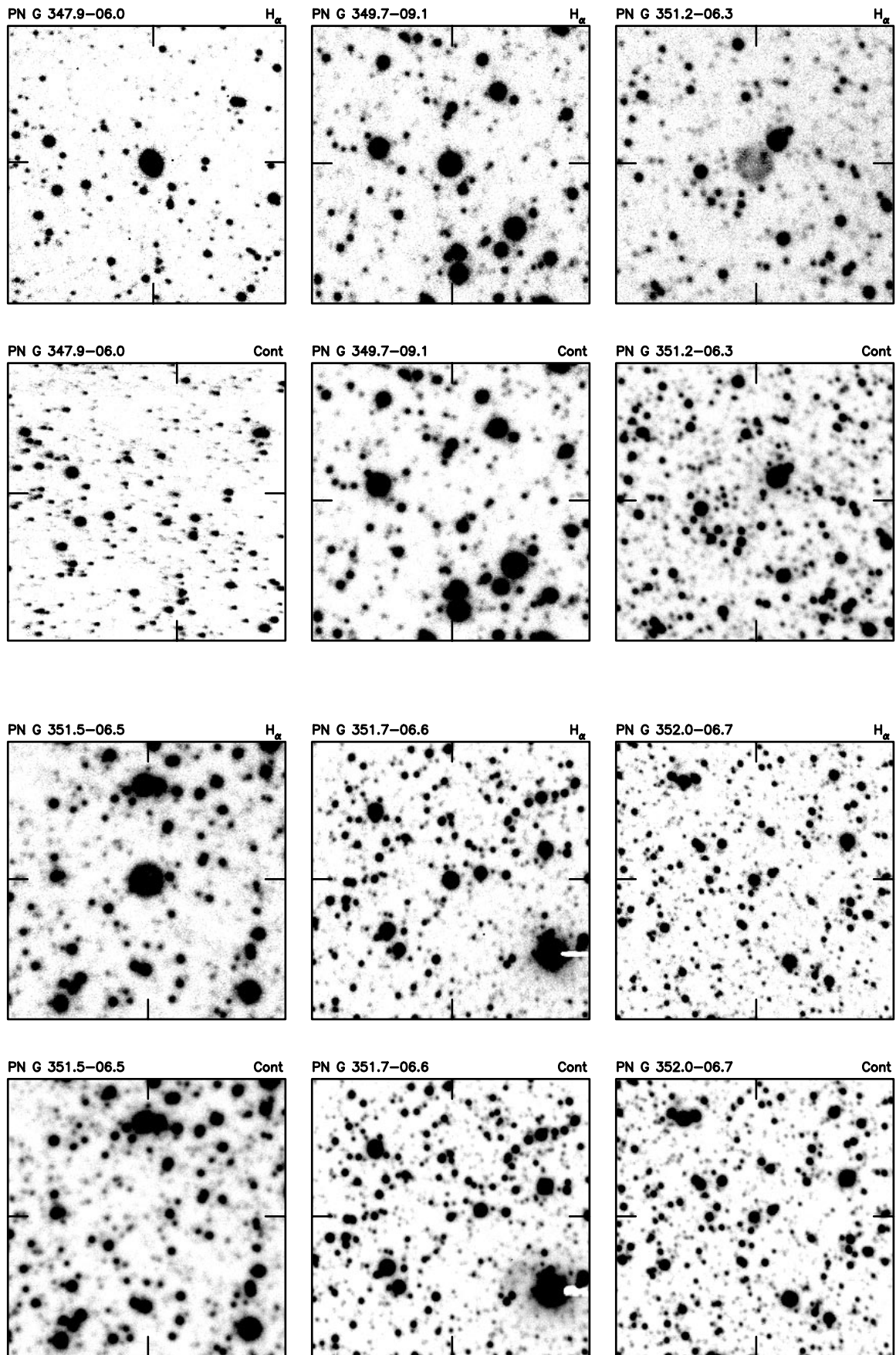


FIG. 6f

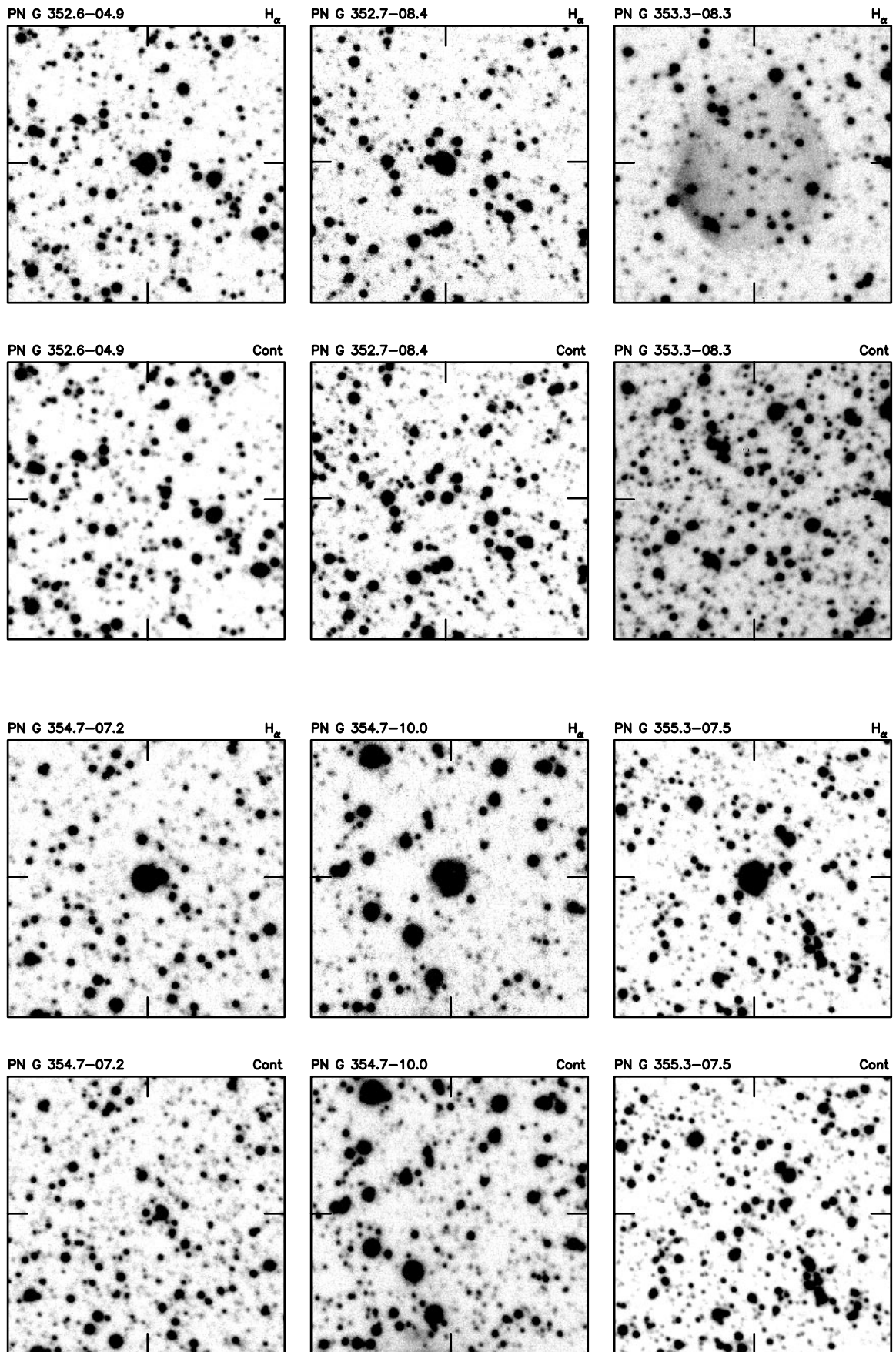


FIG. 6g

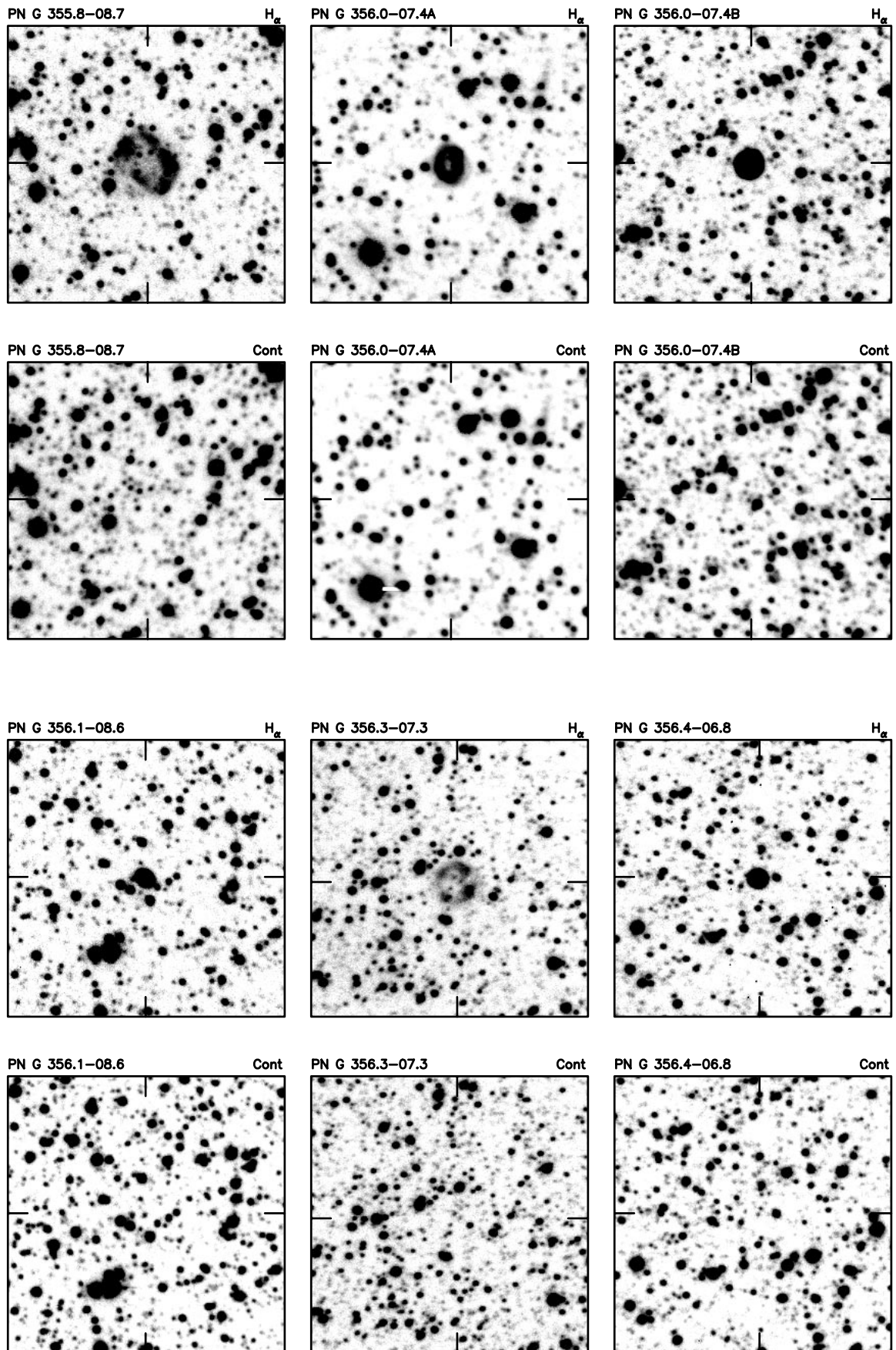


FIG. 6h

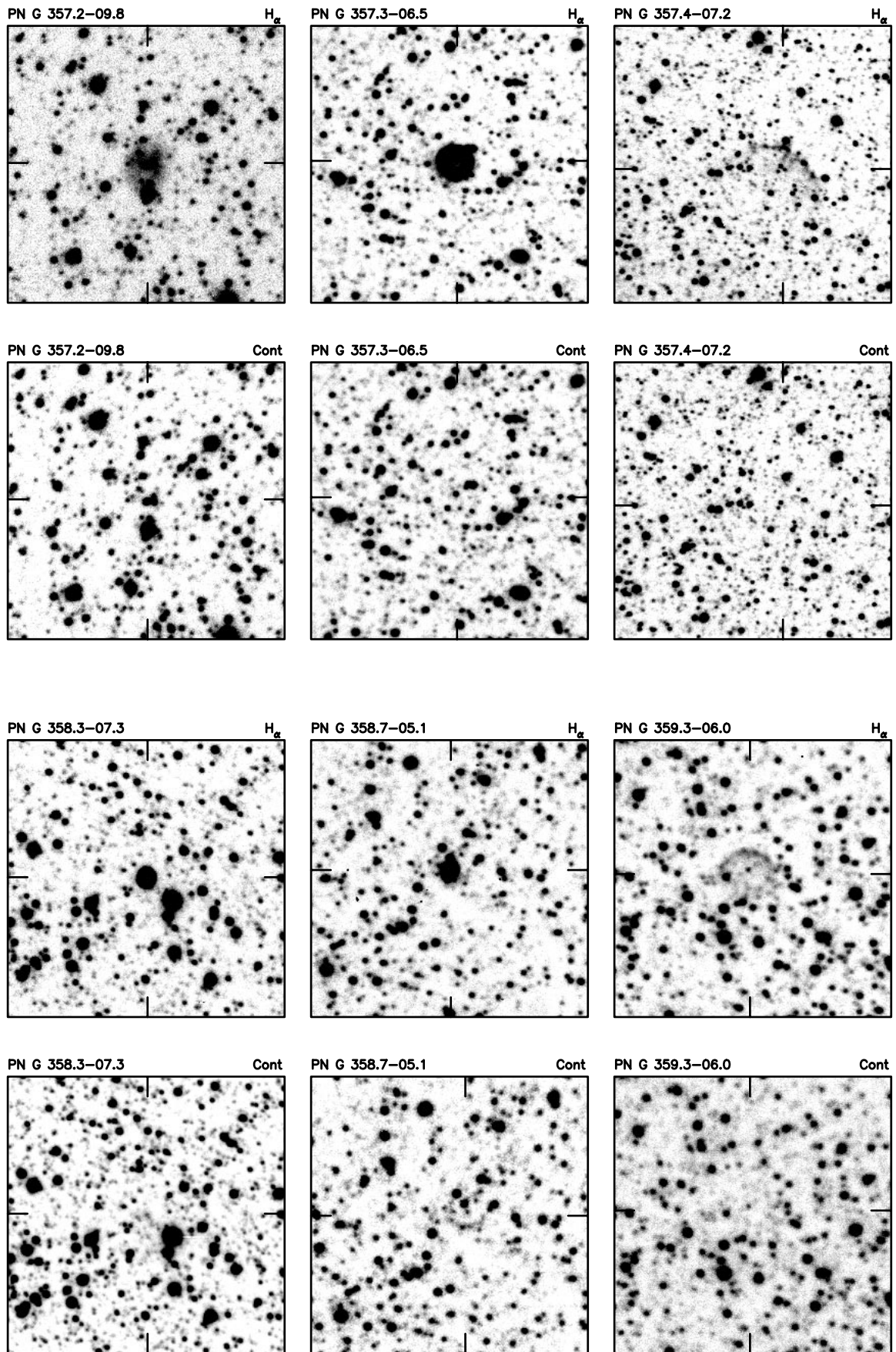


FIG. 6i

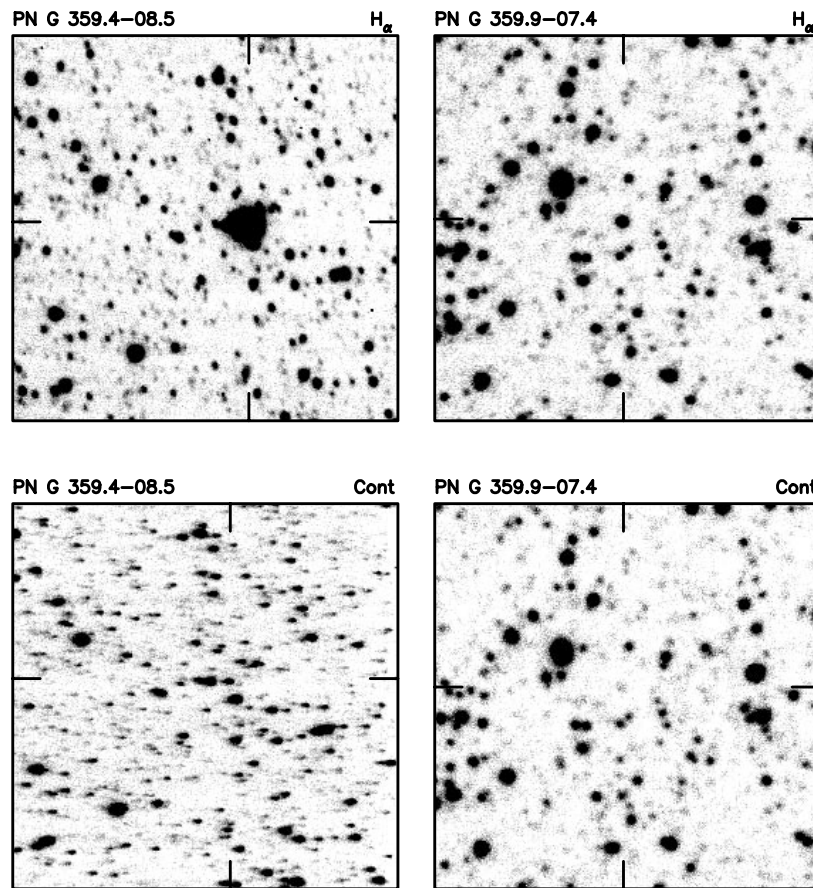


FIG. 6j

continuum images using the worse image as the reference image, then, instead of dividing the $H\alpha$ image by the scaled continuum, we subtracted it. We then measured the total $H\alpha$ counts within a box surrounding the PN. To obtain the absolute flux, we first scaled the flux to a 1 s exposure, corrected for the mean extinction in $H\alpha$ (assuming a coefficient of $0.122 \text{ mag airmass}^{-1}$), and applied a zero point obtained from standards observed each night (also scaled to a 1 s exposure and corrected for the mean extinction). The standard PNs used were PN 003.1+02.9, used in the 1995 season, and PN 321.3-16.7, observed in the 1996 season. PN 321.3-16.7 is one of the Dopita & Hua (1997) flux standards. PN 003.1+02.9 was observed separately by Dopita and Hua, and scaled to the flux system of the other standard PN in their paper (Dopita & Hua 1997). In Table 10, we present $H\alpha$ flux values for 47 of our 56 newly discovered PNs (nine PNs had nonphotometric data and are marked with ellipses). We also give values for the PN diameter (the nonphotometric data as well) in arcseconds for both major and minor axes, since most of our PNs are not circular. We define our diameter as being the position where the total emission drops to the sky level. Thus those diameters may not be appropriate for studying the evolution of the nebula or to determine the PN distance. The values for the diameters and $H\alpha$ fluxes were obtained from the 2.3 m $H\alpha$ images and are therefore considered upper limits. In Table 10 we can find the name of the object (col. [1]), the (l , b) coordinates (col. [2]), the diameter of the PN in arcseconds (col. [3]), and the $H\alpha$ flux in $\log(\text{ergs cm}^{-2} \text{ s}^{-1}$; col. [4]).

This method of subtracting the continuum worked well in most cases but caused problems in a few. The main problem was to match the PSF perfectly in both the $H\alpha$ and the continuum images. The IRAF task used to perform this step is PSFMATCH and does not always work well, because it only uses a single star to model the PSF. The use of a few stars to model the PSF would be preferable.

Most PNs that do not have a visible star within the nebula give almost no continuum. Therefore, as a check, we chose a few PNs that showed no visible stars within their nebula and subtracted the mode of the sky from the $H\alpha$ image only. When we compared their fluxes with the continuum subtracting method, we saw a negligible difference, $\approx 0.005 \text{ mag}$ in between both fluxes.

Figure 7 show a histogram of the 47 PNs $H\alpha$ fluxes. The overall shape of the luminosity function (LF) is quite similar to that of Acker et al. (1992, their Fig. 9a) after adjusting for the $H\alpha/H\beta$ decrement.

4.2. Detection Limit

Using both the 1.0 and 2.3 m data, we have estimated the 1.0 m survey detection limit. For detection of extended objects against the sky, then, $S/N = F_{\text{PN}} / \{F_{\text{PN}} + [N \times (S + \text{RON}^2)]\}^{1/2}$, where F_{PN} is the PN signal—i.e., the number of analog-to-digital units (adu) integrated over the PN (gain of 1)— S is the sky surface brightness in adu pixel^{-1} , N is the area in pixels of the PN, and RON is the readout noise pixel^{-1} .

We now estimate the typical detection limit for the 1.0 m survey, adopting a 5σ detection as limiting. Our PNs have

TABLE 10
PHOTOMETRY OF THE NEW DISCOVERIES

Object	PN G (<i>lll.l ± bb.b</i>)	Diameter (arcsec)	$\log(F_{H\alpha})$ ($\text{ergs cm}^{-2} \text{s}^{-1}$)	Object	PN G (<i>lll.l ± bb.b</i>)	Diameter (arcsec)	$\log(F_{H\alpha})(F_{H\alpha})$ ($\text{ergs cm}^{-2} \text{s}^{-1}$)
SB1	000.1 – 08.0	29.4 × 28.8	–12.422	SB29	343.7 – 09.6	9.0 × 8.4	–13.235
SB2	000.5 – 05.3	26.4 × 24.0	–11.876	SB30	343.9 – 05.8	12.6 × 12.0	–12.059
SB3	000.7 – 06.1	77.4 × 55.2	–11.432	SB31	347.9 – 06.0	13.8 × 16.8	–12.080
SB4	001.1 – 06.4	28.2 × 33.0	...	SB32	349.7 – 09.1	16.2 × 15.0	–12.836
SB5	001.3 – 05.6	21.6 × 19.8	...	SB33	351.2 – 06.3	22.2 × 18.0	–13.054
SB6	001.6 – 05.9	26.4 × 19.8	...	SB34	351.5 – 06.5	21.0 × 22.8	–12.570
SB7	003.3 – 06.1	10.2 × 6.0	...	SB35	351.7 – 06.6	13.2 × 13.2	–12.391
SB8	004.2 – 05.2	22.2 × 31.2	–12.339	SB36	352.0 – 06.7	7.8 × 7.2	–12.459
SB9	004.6 – 09.9	13.2 × 13.2	–13.162	SB37	352.6 – 04.9	10.8 × 13.2	...
SB10	004.7 – 05.5	63.0 × 70.8	–12.961	SB38	352.7 – 08.4	14.4 × 15.6	–12.643
SB11	005.2 – 05.9	10.8 × 10.8	–13.454	SB39	353.3 – 08.3	95.4 × 103.2	–11.951
SB12	005.4 – 06.1	9.6 × 10.8	–13.651	SB40	354.7 – 07.2	18.6 × 20.4	–12.134
SB13	006.5 – 05.8	36.6 × 37.8	...	SB41	354.7 – 10.0	25.8 × 23.4	–12.697
SB14	007.7 – 05.3	19.2 × 18.6	–13.007	SB42	355.3 – 07.5	21.0 × 21.0	–11.934
SB15	009.3 – 06.5	13.8 × 14.4	–12.630	SB43	355.8 – 08.7	40.2 × 42.0	–12.344
SB16	009.4 – 05.6	32.4 × 35.4	–12.934	SB44	356.0 – 07.4A	25.8 × 28.2	–12.322
SB17	011.1 – 07.9	19.8 × 19.2	–12.401	SB45	356.0 – 07.4B	22.2 × 22.2	–12.110
SB18	011.4 – 07.3	12.6 × 11.4	–12.908	SB46	356.1 – 08.6	14.4 × 14.4	–12.387
SB19	014.4 – 06.1	21.6 × 44.4	–11.903	SB47	356.3 – 07.3	30.6 × 28.8	–12.582
SB20	014.8 – 08.4	22.8 × 22.8	–11.942	SB48	356.4 – 06.8	15.0 × 13.8	–12.574
SB21	016.0 – 07.6	24.0 × 24.6	–11.760	SB49	357.2 – 09.8	29.4 × 29.4	–12.957
SB22	016.7 – 07.3	7.8 × 7.8	–13.107	SB50	357.3 – 06.5	24.6 × 22.8	–12.055
SB23	017.5 – 07.4	5.4 × 5.4	–13.315	SB51	357.4 – 07.2	45.6 × 33.0	–12.802
SB24	017.5 – 09.2	18.0 × 19.8	–12.893	SB52	358.3 – 07.3	13.8 × 15.6	–11.818
SB25	341.0 + 09.4	16.2 × 15.6	–12.643	SB53	358.7 – 05.1	14.4 × 16.8	–12.289
SB26	341.7 – 06.0	11.4 × 11.4	–12.422	SB54	359.3 – 06.0	35.4 × 30.0	...
SB27	341.9 + 08.8	10.8 × 12.0	–12.831	SB55	359.4 – 08.5	16.2 × 13.8	–11.801
SB28	342.3 – 06.0	9.0 × 7.8	...	SB56	359.9 – 07.4	6.0 × 5.4	...

a range of diameters, and the sky conditions varied during the survey in the sense that the sky was not always perfectly dark and most of our nights were nonphotometric. We use the above equation to estimate the limiting flux for a set of our PNs, taking the diameter of each PN, the prevailing sky brightness, and the RON of the CCD. We do not take into account variations in the reddening and Galactic background.

For this estimate, we used 45 PNs out of the 47 with 2.3 m photometry: two PNs were too close to the edge of the field of the 1.0 m images. Each of these 45 PNs gives a value

for the real flux ($\text{ergs cm}^{-2} \text{s}^{-1}$) per 1.0 m a.d.u. Our mean 5σ limiting $\log(\text{flux})$ is -13.6 , with an rms scatter of 0.3; this scatter reflects the variable conditions during the survey and the range of diameters of our PN.

Now, if we assume an $H\alpha/H\beta$ ratio of 2.92, then our 5σ detection limit in $H\alpha$ would correspond to an $H\beta \log(\text{flux})$ of about -14.1 . This is fainter than most PN in the Acker et al. (1992) catalog. In practice, most of the objects in this direction will be strongly affected by reddening, so the apparent flux limit of our survey at $H\beta$ would be even less.

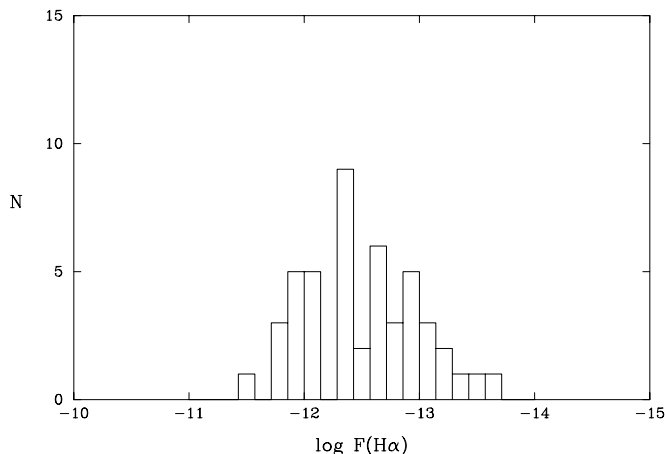


FIG. 7.—Histogram of the $H\alpha$ fluxes for 47 PNs

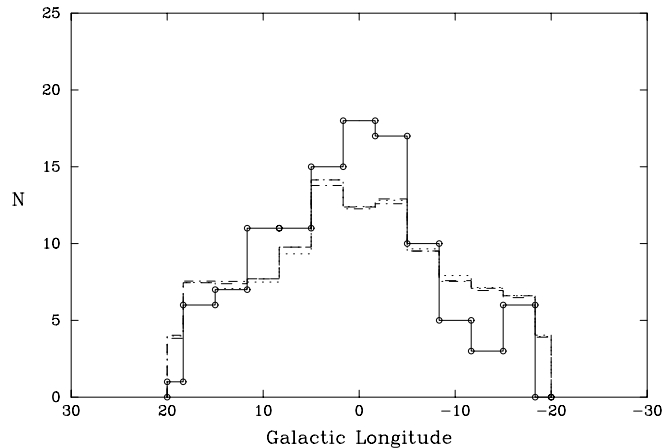


FIG. 8.—Longitude distribution of the COBE light (1.25, 2.2, and 3.5 μm) and the PNs in the survey fields only. The dashed lines represent the three COBE bands, and the solid line is the PNs.

4.3. COBE Light and Dust

Figure 8 shows a histogram of the longitude distribution of the COBE light and the PNs in our southern surveyed fields ($-5^\circ < b < -10^\circ$). The dashed lines represent the three bands (1.25, 2.2, and $3.5\mu\text{m}$) of the COBE light distribution, and the solid line represents the PNs distribution. We see immediately that the three COBE distributions agree very well and that the PNs distribution follows the COBE light distribution. The fact that the three COBE light distributions agree so well is an indication that the extinction in our surveyed fields is not severe and that its distribution is fairly uniform.

5. CONCLUSION

We have reported the results of a deep and uniform narrowband $\text{H}\alpha$ survey for PNs in the Galactic bulge. The goal of the survey was to obtain a sample of bulge tracers, which could then be used to study the dynamics of the Milky Way bulge (Beaulieu et al. 1998).

PNs are good tracers for a dynamical study of the Galactic bulge, because they are less affected by metallicity bias than most other tracers and are strong emitters in $\text{H}\alpha$; this make their velocities easy to measure. We chose to survey the southern Galactic bulge in the region $l = \pm 20^\circ$ and from $b = -5^\circ$ to -10° because of its lower extinction relative to the northern bulge.

We used a 1.0 m telescope with the LDSS as a focal reducer (without grism) to conduct the optical imaging survey. In our survey, we have found 56 new PNs and rediscovered 45 known PNs. We have measured the radial velocities of this uniformly selected sample, which was the basis of the comparison with the dynamical models.

We have also remeasured radial velocities for a subset of 317 catalogued PNs, in a more extended region of $l = \pm 30^\circ$ and $b = \pm(3.3$ and $15^\circ)$: this larger sample will be use for some dynamical comparisons, although the discovery process for this larger sample is less homogeneous.

We compared the longitude distribution of PNs in our surveyed fields with the COBE light distribution at 1.25, 2.2, and $3.5\mu\text{m}$. We conclude that (1) the light distributions in the three COBE bands agree very well, indicating that the extinction in our surveyed fields is not severe and that its distribution is fairly uniform, and (2) there is no significant

difference between the longitude distribution of the PNs and the COBE light in the zone of our deep survey.

Using a 2.3 m telescope, we have obtained $\text{H}\alpha$ fluxes for 47 of our 56 newly discovered PNs. The LF is very similar to the one presented by Acker et al. (1992, their Fig. 9a) after adjusting for the $\text{H}\alpha/\text{H}\beta$ decrement. Then, using the 1.0 and 2.3 m data, we have estimated our 1.0 m $\text{H}\alpha$ survey detection limit to be $\log F(\text{H}\alpha) = -13.6$ ergs $\text{cm}^{-2} \text{s}^{-1}$.

The PNs of the Galactic bulge constitute the largest and nearest population of PNs. Our survey has doubled the number of known PNs in the surveyed region. If the LF of PNs in the direction of the Galactic bulge increases in the way Jacoby (1982) suggested was the case for LMC PNs, then our survey should have found at least 200 new objects, but we found only 56.

There are three possibilities for this lack of PNs: it could be that the PNs are dust-enshrouded because of their high metallicity or that the PNs are associated with a low-mass central star, so that the nebula has expanded and become optically thin in the timescale over which the central star becomes hot enough to ionize it. Our survey may not have been deep enough to pick them up. A third possibility could be that the pressure in the hot phase of the interstellar medium in the bulge region is so high that ram-pressure can strip the PN shell away from the central star in a timescale that is short compared with the fading timescale of central star. We will investigate this possibility in more detail in another publication.

An $\text{H}\alpha$ survey of the southern Galactic plane is now well underway at the AAO United Kingdom Schmidt Telescope Unit, using the newly acquired interference filter with fine-grained Kodak TechPan film. The survey will cover 233×4 deg² Galactic plane fields with overlap. Typical 3 hr exposures have already yielded about 30 PNs candidates on 10 scanned plates (Parker & Phillips 1998).

S. F. B. wish to acknowledge funding from The Australian Government through an Australian National University Scholarship and an Overseas Postgraduate Research Scholarship. We wish to thank the AAO for lending us the LDSS. We are grateful to Don Matheson, Vince Ford, Bill Roberts, and Stéphane Vennes for giving up much needed observing time.

REFERENCES

- Acker, A., Marcout, J., Ochsenbein, F., Beaulieu, S., García-Lario, P., & Jacoby, G. 1996, First Supplement to the Strasbourg-ESO Catalogue of Galactic Planetary Nebulae (Strasbourg: Obs. Strasbourg)
- Acker, A., Ochsenbein, F., Stenholm, B., Tylenda, R., Marcout, J., & Schohn, C. 1992, in The Strasbourg-ESO Catalogue of Galactic Planetary Nebulae, Parts 1 and 2 (Strasbourg: ESO)
- Beaulieu, S. F. 1996, PhD thesis, Australian Natl. Univ.
- Beaulieu, S. F., Kalnajs, A. J., & Freeman, K. C. 1998, in preparation
- Dopita, M. A., & Hua, C. T. 1997, *ApJS*, 108, 515
- Gilliland, R. L. 1992, ASP Conf. Ser. 23, Astronomical CCD Observing and Reduction Techniques, ed. S. B. Howell (San Francisco: ASP), 68
- IRAS Point Source Catalog, Version 2. 1988, Joint IRAS Science Working Group (Washington, DC: GPO)
- Jacoby, G. H. 1982, IAU Symp. 103, Planetary Nebulae, ed. D. R. Flower (Dordrecht: Kluwer), 427
- Madsen, C., & Laustsen, S. 1986, *Messenger*, 46, 12
- Massey, P. 1992, A User's Guide to CCD Reduction with IRAF (Tucson: NOAO)
- Massey, P., Valdes, F., & Barnes, J. 1992, A User's Guide to Reducing Slit Spectra with IRAF (Tucson: NOAO)
- Menzel, D. H. 1960, *Fundam. Formulas Phys.*, 1, 140
- Minkowski, R. 1965, in Stars and Stellar System: Galactic Structure, Vol.5, ed. A. Blaauw & M. Schmidt (Chicago: Univ. Chicago Press), 321
- Parker, Q. A., & Phillips, S. 1998, *Proc. Astron. Soc. Australia*, 15, 28
- Pottasch, S. R. 1992, *A&A Rev.*, 4, 215
- Pottasch, S. R., Bignell, C., Olling, R., & Zijlstra, A. A. 1988, *A&A*, 205, 248
- Ratag, M. A. 1990, Ph.D. thesis, Univ. Groningen
- van de Steene, G. C. 1995, Ph.D. thesis, Univ. Groningen
- Weiland, J. L., et al. 1993, in AIP Conf. Proc. 278, Back to the Galaxy, ed. S. S. Holt & F. Verter (New York: AIP), 137
- Wyse, R. F. G., Gilmore, G., & Franx, M. 1997, *ARA&A*, 35, 637